The Astrophysical Journal, 791:52 (23pp), 2014 August 10 doi:10.1088/0004-637X/791/1/52

CANDELS+3D-HST: COMPACT SFGs AT $z \sim 2$–3, THE PROGENITORS OF THE FIRST QUIESCENT GALAXIES

G. Barro[1], S. M. Faber[1], P. G. Pérez-González[2,3], C. Pacifici[4], J. R. Trump[5], D. C. Koo[1], S. Wuyts[6], Y. Guo[1], E. Bell[7], A. Dekel[8], L. Porter[9], J. Primack[9], H. Ferguson[10], M. L. N. Ashby[11], K. Caputi[12], D. Ceverino[13], D. Croton[14], G. G. Fazio[11], M. Giavalisco[15], L. Hsu[6], D. Kocevski[16], A. Koekemoer[10], P. Kurczynski[17], P. Kollipara[9], J. Lee[4], D. H. McIntosh[18], E. McGrath[19], C. Moody[9], R. Somerville[17], C. Papovich[20], M. Salvato[6], P. Santini[21], T. Tal[1], A. van der Wel[22], C. C. Williams[15], S. P. Willner[11], and A. Zolotov[8]

[1] UCO/Lick Observatory and Department of Astronomy and Astrophysics, University of California, Santa Cruz, CA 95064 USA
[2] Universidad Complutense de Madrid, F. CC. Físicas, 28040 Madrid, Spain
[3] Associate Astronomer at Steward Observatory, 933 North Cherry Street, University of Arizona, Tucson, AZ 85721, USA
[4] Yonsei University Observatory, Yonsei University, Seoul 120-749, Republic of Korea
[5] Pennsylvania State University, University Park, PA 16802 USA
[6] Max-Planck-Institut für extraterrestrische Physik, Postfach 1312, Giessenbachstr., D-85741 Garching, Germany
[7] Department of Astronomy, University of Michigan, Ann Arbor, MI 48109 USA
[8] Racah Institute of Physics, The Hebrew University, Jerusalem 91904, Israel
[9] Santa Cruz Institute for Particle Physics, University of California, Santa Cruz, CA 95064, USA
[10] Space Telescope Science Institute, 3700 San Martin Drive, Baltimore, MD 21218, USA
[11] Harvard-Smithsonian Center for Astrophysics, 60 Garden Street, Cambridge, MA 02138, USA
[12] Kapteyn Astronomical Institute, University of Groningen, P.O. Box 800, 9700 AV Groningen, The Netherlands
[13] Departamento de Física Teórica, Universidad Autónoma de Madrid, 28049 Madrid, Spain
[14] Centre for Astrophysics and Supercomputing, Swinburne University of Technology, PO Box 218, Hawthorn, VIC 3122, Australia
[15] Astronomy Department, University of Massachusetts, 710 North Pleasant Street, Amherst, MA 01003, USA
[16] Department of Physics and Astronomy, University of Kentucky, Lexington, KY, 40506, USA
[17] Department of Physics and Astronomy, Rutgers University, Piscataway, NJ 08854, USA
[18] Department of Physics & Astronomy, University of Missouri-Kansas City, 5110 Rockhill Road, Kansas City, MO 64110, USA
[19] Department of Physics and Astronomy, Colby College, Waterville, ME 04901, USA
[20] Department of Physics and Astronomy, Texas A&M University, College Station, TX 77843, USA
[21] INAF-Osservatorio Astronomico di Roma, Via Frascati 33, I-00040, Monteporzio, Italy
[22] Max-Planck-Institut für Astronomie, Königstuhl 17, D-69117 Heidelberg, Germany
Received 2013 November 15; accepted 2014 June 14; published 2014 July 25

ABSTRACT

We analyze the star-forming and structural properties of 45 massive ($\log(M/M_\odot) > 10$) compact star-forming galaxies (SFGs) at $2 < z < 3$ to explore whether they are progenitors of compact quiescent galaxies at $z \sim 2$. The optical/NIR and far-IR *Spitzer*/*Herschel* colors indicate that most compact SFGs are heavily obscured. Nearly half (47%) host an X-ray-bright active galactic nucleus (AGN). In contrast, only about 10% of other massive galaxies at that time host AGNs. Compact SFGs have centrally concentrated light profiles and spheroidal morphologies similar to quiescent galaxies and are thus strikingly different from other SFGs, which typically are disk-like and sometimes clumpy or irregular. Most compact SFGs lie either *within* the star formation rate (SFR)–mass main sequence (65%) or *below* it (30%), on the expected evolutionary path toward quiescent galaxies. These results show conclusively that galaxies become more compact before they lose their gas and dust, quenching star formation. Using extensive *HST* photometry from CANDELS and grism spectroscopy from the 3D-HST survey, we model their stellar populations with either exponentially declining (τ) star formation histories (SFHs) or physically motivated SFHs drawn from semianalytic models (SAMs). SAMs predict longer formation timescales and older ages ~2 Gyr, which are nearly twice as old as the estimates of the τ models. Both models yield good spectral energy distribution fits, indicating that the systematic uncertainty in the age due to degeneracies in the SFH is of that order of magnitude. However, SAM SFHs better match the observed slope and zero point of the SFR–mass main sequence. Contrary to expectations, some low-mass compact SFGs ($\log(M/M_\odot) = 10$–10.6) have younger ages but lower specific SFRs than that of more massive galaxies, suggesting that the low-mass galaxies reach the red sequence faster. If the progenitors of compact SFGs are extended SFGs, state-of-the-art SAMs show that mergers and disk instabilities (DIs) are both able to shrink galaxies, but DIs are more frequent (60% versus 40%) and form more concentrated galaxies. We confirm this result via high-resolution hydrodynamic simulations.

Key words: galaxies: high-redshift – galaxies: photometry – galaxies: starburst

Online-only material: color figures

1. INTRODUCTION

The formation history of very massive galaxies is not well understood. Present-day massive galaxies are known to be a homogeneous population characterized by red optical colors that follow a tight correlation with stellar mass (i.e., the red sequence; Kauffmann et al. 2003; Baldry et al. 2004). This population consists mostly of galaxies with early-type morphologies and passively evolving stellar populations (e.g., Djorgovski & Davis 1987; Thomas et al. 2005). However, a coherent evolutionary picture of their early star formation histories (SFHs) and the buildup of their stellar mass over cosmic time is still lacking.

Observations at higher redshifts suggest that the first quiescent galaxies formed very early during the first 2–3 Gyr of the universe, becoming the dominant population among massive galaxies as early as $z \sim 2$ (Fontana et al. 2009; Ilbert et al.

2010; Brammer et al. 2011; Muzzin et al. 2013). Recent works have even identified, photometrically and spectroscopically, a small number of these galaxies at $z \sim 3$–4 (Guo et al. 2011; Gobat et al. 2012; Stefanon et al. 2013), indicating that a fraction of the quiescent population appears in only ∼1 Gyr. What is perhaps even more surprising is that the first quiescent galaxies were structurally very different from their local analogs, having effective radii up to a factor of ∼3–5 smaller than those of quiescent galaxies at $z \sim 0$ (e.g., Daddi et al. 2005; van Dokkum et al. 2008; Trujillo et al. 2007; Buitrago et al. 2008; Toft et al. 2007; Saracco et al. 2010; Cassata et al. 2011; Szomoru et al. 2011).

Theoretical models are slowly converging on an evolutionary picture that describes the formation of quiescent galaxies as a two-stage process (e.g., Naab et al. 2007; Oser et al. 2010). First, an early phase of highly dissipative in situ star formation fueled by cold gas streams (Birnboim & Dekel 2003; Kereš et al. 2005; Dekel & Birnboim 2006; Dekel et al. 2009a) or gas-rich mergers (Hopkins et al. 2006; Hopkins et al. 2008) leads to the formation of a compact remnant (Elmegreen et al. 2008; Dekel et al. 2009b; Wuyts et al. 2010). Then, a late phase of size growth dominated by the accretion of smaller systems slowly increases their radii (Bournaud et al. 2007; Naab et al. 2009; Bezanson et al. 2009; although for a different picture see Poggianti et al. 2013; Carollo et al. 2013). One of the main challenges of this picture is identifying the mechanism responsible for both the truncation of the star formation and the structural transformation to understand the relation between the quiescent population and their star-forming progenitors. Indeed, observations reveal that these two populations have significantly different structural properties at $z \gtrsim 2$. While star-forming galaxies (SFGs) exhibit disk-like morphologies and, in many cases, irregular and clumpy structures (e.g., Elmegreen & Elmegreen 2005; Elmegreen et al. 2007; Kriek et al. 2009a; Guo et al. 2012), quiescent galaxies at that redshift are spheroid dominated (Szomoru et al. 2011; Bell et al. 2012). Furthermore, quiescent galaxies have smaller sizes than SFGs of the same stellar mass (Williams et al. 2010; Wuyts et al. 2011a). This difference suggests that the observational picture is missing a key population in the evolutionary sequence that connects star-forming and quiescent galaxies, namely, objects transitioning from star-forming to quiescent that simultaneously experience a shrinkage in size.

Naively one would expect that such a connection would be through a population of massive, compact SFGs. However, evidence for such galaxies remained elusive even for the deepest *Hubble Space Telescope* (*HST*) optical surveys, which can only probe the rest-frame UV of $z \gtrsim 1.5$ galaxies and thus tend to miss dust-obscured galaxies. Now, owing to new IR capabilities of the WFC3 camera, the analysis of (rest-frame optical) sizes can be extended to higher redshifts, and evidence has started to accumulate, revealing the existence of an abundant population of compact but red SFGs at $z \sim 2$–3 (Wuyts et al. 2011b; Patel et al. 2013; Barro et al. 2013; Stefanon et al. 2013; Williams et al. 2014). These galaxies typically have large stellar masses, heavily obscured star formation, and spheroid-like morphologies. More importantly, they exhibit the small radii of compact quiescent galaxies, implying that structural changes can occur on timescales comparable to the star formation quenching timescale.

Barro et al. (2013, hereafter B13) demonstrated that the radii and stellar mass surface densities of compact SFGs quantitatively matched those of compact quiescent galaxies. They further showed that the fall in the number density of compact SFGs since $z \sim 3$ is consistent with the observed increase in the density of compact quiescent galaxies assuming quenching times for the former of 300 Myr to 1 Gyr. Relatively short star formation timescales are plausible if, as pointed out in Wuyts et al. (2011b), some of these galaxies are offset from the star formation rate (SFR)$-M_\star$ correlation (the so-called main sequence; Noeske et al. 2007; Elbaz et al. 2007) toward the high-SFR upper envelope. In such extreme cases, gas exhaustion, supernova, and active galactic nucleus (AGN) feedback lead to a rapid decline in SFR. The latter can be particularly relevant in compact galaxies sustaining large SFRs over very small regions. As shown in, e.g., Diamond-Stanic et al. (2012) (see also Tremonti et al. 2007; Newman et al. 2014b), high SFR surface densities are associated with strong galactic outflows that can deplete the gas reservoirs in a short period of time.

Understanding the location and evolution of compact SFGs in relation to the main sequence of "normal" galaxies is critical to assess whether they represent extreme cases of high star formation efficiency (*starburst*; Daddi et al. 2010; Rodighiero et al. 2010) such as submillimeter galaxies and hyper luminous infrared galaxies (Smail et al. 1997; Blain et al. 2002; Targett et al. 2013), or if they are forming stars gradually over longer timescales. Life paths on this diagram allow us to explore the proposed evolutionary connection with quiescent galaxies, as well as discriminate between possible formation scenarios that predict different trends in the structural properties, the morphological type, or the amount of dust extinction along the evolutionary track.

The aim of this paper is to extend the results of B13 and present further evidence that compact SFGs at $2 < z < 3$ are the natural progenitors of compact quiescent galaxies at $z \sim 2$. To that end, we present a detailed analysis of a sample of 45 compact SFGs, selected from the CANDELS survey in GOODS-S. First, we assemble comprehensive UV-to-far-IR spectral energy distributions (SEDs) for these galaxies, and we study their observed and rest-frame colors, SFRs, morphologies, structural properties, and AGN activity with respect to other star-forming and quiescent galaxies at the same redshift. Then, we model their SEDs using stellar population synthesis to (1) estimate their stellar ages, (2) study the implications of the assumed SFH on the predicted tracks in the SFR–M diagram and compare these with the observed galaxy distribution, and (3) estimate their quenching times and compare the predicted number of quenched compact SFGs as a function of time with the observed number density of quiescent galaxies since $z = 3$. Finally, we speculate on the origin of compact SFGs by studying their possible formation mechanisms using semianalytic models (SAMs) and *N*-body simulations.

The structure of the paper is as follows. In Section 2 we describe the data sets, the SED modeling, the procedure to estimate galaxy properties and the criteria to select compact SFGs. In Section 3 we study the SFRs, optical/near-IR (NIR)/far-IR colors, structural properties, and AGN activity of these galaxies. In Section 4 we compare the best-fit stellar ages and formation timescales for compact SFGs obtained with three different SFH models. In Section 5 we show the evolutionary tracks in the SFR–*M* and *UVJ* diagrams inferred from their SFHs, and we discuss the implications for the proposed evolutionary sequence from star-forming to quiescent. In Section 6 we discuss the formation mechanisms of compact SFGs in the context of theoretical simulations.

Throughout the paper we adopt a flat cosmology with $\Omega_M = 0.3$, $\Omega_\Lambda = 0.7$, and $H_0 = 70$ km s^{-1} Mpc^{-1}, and we quote magnitudes in the AB system.

2. DATA

The sample of compact SFGs analyzed in this paper is drawn from the parent catalog presented in B13. In the following, we briefly outline the data sets on which the catalog is based, the procedures to estimate stellar properties and SFRs, and the most relevant over B13.

2.1. Multiband Photometric Data in GOODS-S/CANDELS

The parent galaxy sample is derived from an *HST*/WFC3 F160W (H-band) selected catalog in the GOODS-S field. The WFC3/IR observations in this field cover a total area of $\sim$173 arcmin^2 at different depths. The Early Release Science (Windhorst et al. 2011) and the CANDELS Wide regions (Grogin et al. 2011; Koekemoer et al. 2011) cover $\sim$2/3 of the area at two-orbit depth ($H_{5\sigma} = 27.4$ mag; 115 arcmin^2), and the CANDELS Deep region covers the remaining 1/3 at 10 orbit depth ($H_{5\sigma} = 28.2$ mag; 55 arcmin^2). The galaxies were selected from a combined mosaic drizzled to a 0.″06 pixel^{-1} scale with a typical point-spread function (PSF) of $\sim$0.″18. The multiwavelength catalog based on the H-band selection includes photometry in 14 passbands ranging from U to 8 μm, with seven high-resolution bands from *HST*/Advanced Camera for Surveys (ACS) and WFC3 (B_{435}, V_{606}, i_{775}, z_{850}, YJH) and the deepest *Spitzer*/IRAC data from SEDs (Ashby et al. 2013). The merging with lower-resolution data (ground based and *Spitzer*/IRAC) was computed using TFIT (Laidler et al. 2006). A comprehensive overview of this catalog can be found in Guo et al. (2013; see also Galametz et al. (2013) for more details).

We also include complementary mid-IR photometry in *Spitzer*/MIPS 24 and 70 μm (30 μJy and 1 mJy, 5σ) from Pérez-González et al. (2008b), and far-IR from the GOODS-*Herschel* (Elbaz et al. 2011) and PEP (Magnelli et al. 2013) surveys, including PACS 100 and 160 μm and SPIRE 250, 350, and 500 μm. A description of the method used to derive consistent mid- to far-IR SEDs is presented in Pérez-González et al. (2008a, 2010). X-ray source identifications and total luminosities ($L_X \equiv L_{2-8\,\mathrm{kev}}$) were computed for the sources identified in the *Chandra* 4 Ms catalog (Xue et al. 2011).

2.2. Inferred Galaxy Properties

In order to select a sample of compact SFGs, we first derive photometric redshifts, stellar masses, and SFRs for all the galaxies in the H-band-selected catalog from SED modeling. These properties have been used in previous works by Wuyts et al. (2011b, 2012) and B13. Therefore, we describe here only the most relevant details. In brief, photometric redshifts were estimated from a variety of different codes available in the literature, which are then combined to improve the individual performance. The technique is fully described in Dahlen et al. (2013), and the catalog will be released in T. Dahlen et al. (2014, in preparation). Based on the best available redshifts (spectroscopic or photometric; see Table 1), we estimated stellar masses and other stellar population properties (such as age, extinction, and UV-based SFR) using FAST (Kriek et al. 2009b). The modeling is based on a grid of Bruzual & Charlot (2003, BC03) models that assume a Chabrier (2003) initial mass function (IMF), solar metallicity, exponentially declining SFHs, and a Calzetti et al. (2000) extinction law. Rest-frame magnitudes based on the best-fit redshifts and stellar templates were computed using EAZY (Brammer et al. 2008).

We compute SFRs on a galaxy-by-galaxy basis using a *ladder* of SFR indicators as described in Wuyts et al. (2011a). The method essentially relies on IR-based SFR estimates for galaxies detected at mid- to far-IR wavelengths, and SED-modeled SFRs for the rest. As shown in Wuyts et al. (2011a), the agreement between the two estimates for galaxies with a moderate extinction (faint IR fluxes) ensures the continuity between the different SFR estimates (see also Appendix B). For IR-detected galaxies the total SFRs, $\mathrm{SFR_{IR+UV}}$, were then computed from a combination of IR and rest-frame UV luminosities (uncorrected for extinction) following Kennicutt (1998) (see also Bell et al. 2005):

$$\mathrm{SFR_{UV+IR}} = 1.09 \times 10^{-10}(L_{\mathrm{IR}} + 3.3L_{2800})\ [M_\odot\ \mathrm{yr}^{-1}]. \quad (1)$$

The normalization factor corresponds to a Chabrier (2003) IMF, and L_{2800} is estimated from the best-fitting SED template. Note that for the analysis of compact SFGs we perform a more exhaustive SED modeling in Section 4. However, we base our sample selection on an easy-to-reproduce method using the standard data described above. We verify that the recomputed stellar properties do not introduce any significant difference on the sample selection. The recomputed redshifts changed $<$1% (half the sample is spectroscopically confirmed), and other properties depending only on redshift (r_{eff}, SFR) remained unchanged at the same level. The median change in stellar masses and rest-frame colors is consistent with zero, with a scatter of $\Delta M = 0.03$ dex and $\Delta\mathrm{color} = 0.05$ mag.

The shapes of the two-dimensional surface brightness profiles measured from the *HST*/WFC3 F160W image were modeled using GALFIT (Peng et al. 2002). The method and the catalog are fully described in van der Wel et al. (2012). A single-component fit was performed to determine the circularized, effective (half-light) radius, $r_e \equiv a_{\mathrm{eff}}\sqrt{(b/a)}$ (a_{eff} is the half-light radius along the major axis), and the Sérsic index, n. Spatially variable PSFs were created and processed with TinyTim (Krist 1995) to replicate the conditions of the observed data when fitting light profiles. We note that the circularized radius, although widely used in the literature, may cause edge-on galaxies to appear smaller (see Section 3.3).

2.3. Selection of Compact SFGs

Following the criteria of B13, we select a sample of massive ($M_\star > 10^{10}\,M_\odot$) compact SFGs at $2 < z < 3$, using a threshold in *pseudo*-stellar mass surface density, $\Sigma_{1.5}$, of $\log(M/r_e^{1.5}) > 10.45\,M_\odot$ kpc$^{-1.5}$ (below the black line in Figure 1) and specific SFR $\log(\mathrm{sSFR/Gyr^{-1}}) > -0.75$. The latter is set slightly above a mass doubling time of $3 \times t_{\mathrm{Hubble}}$ at $z \sim 2.5$ to reject the majority of passively evolving galaxies, whereas the limit in $\Sigma_{1.5}$ is chosen to select galaxies in the region of the mass–size diagram occupied by quiescent galaxies at $z > 2$. Based on these criteria, we identify a total of 45 compact SFGs. The overall properties of these galaxies are summarized in Table 1. We note that four of these galaxies are excluded from the analysis of the stellar properties in the following sections (except Section 3.4) due to AGN continuum contamination in the SED (see Appendix A).

To illustrate the motivation of the selection criteria, Figure 1 shows the mass–size relation for galaxies more massive than $\log(M/M_\odot) > 9$ in four redshift intervals in the range

Table 1
Properties of Compact SFGs

ID (1)	R.A. (2)	Decl. (3)	$z_{\rm best}$ (4)	z-REF (5)	X-ray (6)	$f_{24\,\mu{\rm m}}$ (7)	$f_{100\,\mu{\rm m}}$ (8)	$f_{250\,\mu{\rm m}}$ (9)	SFR (10)	Mass (11)	$r_{\rm eff}$ (12)	$U-V$ (13)	$V-J$ (14)	Reg (15)	G141 (16)
21937	53.00658860	−27.72416860	2.726	9	86^{-}	62 ± 6	...	...	17 ± 6	10.21 ± 0.05	0.29 ± 0.01	0.68	0.56	3	A
14781	53.03332780	−27.78257480	2.619	5	137^{-}	81 ± 7	$2206 \pm$	...	192 ± 11	10.60 ± 0.10	1.00 ± 0.04	1.14	1.49	4	A([O II])
23382	53.16229880	−27.71213490	2.433	1,2	534	80 ± 9	...	2175 ± 1723	84 ± 9	11.27 ± 0.08	1.77 ± 0.03	1.73	1.16	2	A
21662	53.05885220	−27.72632930	2.180	...	...	155 ± 8	1838 ± 307	...	341 ± 12	11.22 ± 0.11	2.70 ± 0.20	1.56	1.69	5	B
22069	53.10207860	−27.72256120	2.610	...	...	...	...	...	3 ± 2	10.45 ± 0.06	0.33 ± 0.01	1.53	0.54	1	B
22539	53.18736680	−27.71918680	2.315	1,3	...	...	...	...	10 ± 5	10.88 ± 0.05	0.43 ± 0.01	1.34	0.38	1	A
23896	53.10081420	−27.71598590	2.303	1,2	326	49 ± 9	...	...	32 ± 7	10.87 ± 0.03	1.40 ± 0.05	1.19	0.96	4	A
25998	53.13757210	−27.70010390	2.453	1,2	...	140 ± 7	3359 ± 459	...	365 ± 12	10.90 ± 0.05	0.95 ± 0.03	1.27	1.18	4	A
26056	53.06325870	−27.69964260	2.402	1,9	215	109 ± 7	...	...	97 ± 9	10.75 ± 0.04	1.13 ± 0.05	1.16	1.25	4	B
25879	53.03444580	−27.69821010	2.474	8	138^{-}	37 ± 6	...	...	19 ± 8	10.54 ± 0.07	0.47 ± 0.04	1.10	1.10	4	B
19298	53.01265220	−27.74724370	2.573	9	93	12 ± 7	...	...	25 ± 9	10.76 ± 0.04	0.49 ± 0.02	1.28	0.67	1	B
20659	53.18283880	−27.73491130	2.432	1,2,4	...	72 ± 6	...	...	94 ± 13	10.98 ± 0.06	0.52 ± 0.01	1.05	0.87	4	A
9834	53.14882690	−27.82112070	2.576	7	490^{+}	588 ± 13	5731 ± 460	20669 ± 3241	391 ± 18	11.06 ± 0.07	2.43 ± 0.03	1.42	1.16	4	B
4150	53.05557910	−27.87400810	2.560	3	...	78 ± 10	...	...	160 ± 15	11.28 ± 0.11	2.57 ± 0.10	1.58	0.92	2	...
9290	53.18622010	−27.82519980	2.030	...	...	...	...	...	6 ± 5	10.51 ± 0.06	0.54 ± 0.01	1.27	0.49	1	A
1883	53.16977920	−27.90078740	2.673	4	...	33 ± 5	...	...	86 ± 13	10.37 ± 0.13	0.83 ± 0.03	0.67	0.65	3	C
2644	53.16450380	−27.89038860	2.123	4	544	323 ± 8	...	...	62 ± 12	10.83 ± 0.09	0.82 ± 0.02	0.66	0.47	3	A
536	53.08917740	−27.93046510	2.611	7	294	31 ± 7	...	...	38 ± 11	10.32 ± 0.12	0.41 ± 0.04	0.79	0.78	3	B
580	53.08732350	−27.92954880	2.680	...	290	47 ± 8	...	...	22 ± 9	11.03 ± 0.07	0.82 ± 0.02	1.44	0.59	1	C
18475	53.10810690	−27.75397980	2.728	1,6	359	...	...	...	20 ± 9	10.44 ± 0.22	0.33 ± 0.01	1.28	0.60	1	C
3643	53.07600440	−27.87816150	2.793	8	254	...	...	...	13 ± 7	10.32 ± 0.08	0.33 ± 0.01	0.71	0.63	3	B
20790	53.17444810	−27.73329980	2.576	2	564	7 ± 5	...	...	93 ± 13	10.20 ± 0.10	0.38 ± 0.04	0.76	0.91	3	B
1086	53.13717980	−27.91583650	2.570	...	...	...	...	...	4 ± 4	10.37 ± 0.11	0.42 ± 0.04	1.46	0.54	1	B
19143	53.02794410	−27.74866340	2.300	...	123	...	...	...	12 ± 7	10.57 ± 0.14	1.16 ± 0.09	1.35	1.07	4	B
26659	53.08446670	−27.70418600	2.510	...	...	...	...	...	8 ± 6	10.71 ± 0.12	1.53 ± 0.10	1.48	0.64	1	B
11701	53.09402810	−27.80412630	2.560	...	310^{+}	147 ± 7	792 ± 210	...	442 ± 28	11.16 ± 0.26	1.27 ± 0.04	1.66	1.67	5	B

Table 1
(Continued)

ID (1)	R.A. (2)	Decl. (3)	$z_{\rm best}$ (4)	z-REF (5)	X-ray (6)	$f_{24\,\mu{\rm m}}$ (7)	$f_{100\,\mu{\rm m}}$ (8)	$f_{250\,\mu{\rm m}}$ (9)	SFR (10)	Mass (11)	$r_{\rm eff}$ (12)	$U-V$ (13)	$V-J$ (14)	Reg (15)	G141 (16)
15614	53.14889600	−27.77750460	2.070	...	...	64 ± 8	1193 ± 320	...	35 ± 10	10.20 ± 0.09	0.32 ± 0.01	1.14	1.32	4	A([O III])
26231	53.06500180	−27.70001300	2.500	...	...	...	...	...	12 ± 7	10.24 ± 0.08	0.45 ± 0.01	1.22	0.47	1	B
26211	53.06595180	−27.70185220	2.110	...	...	153 ± 9	1738 ± 558	...	135 ± 14	10.81 ± 0.06	1.12 ± 0.02	1.69	1.09	2	C
25952	53.12113620	−27.69807510	1.970	1	...	91 ± 9	...	...	57 ± 12	10.63 ± 0.07	0.74 ± 0.02	1.13	0.85	4	A
3280	53.06061510	−27.88237230	2.150	...	...	228 ± 8	2724 ± 441	7101 ± 1080	167 ± 15	10.82 ± 0.09	0.61 ± 0.02	1.29	1.13	4	...
26612	53.07743450	−27.70465270	2.080	...	...	40 ± 9	...	...	30 ± 10	10.76 ± 0.06	0.75 ± 0.05	1.31	1.60	4	B
22603	53.10701590	−27.71822560	2.291	1,5	351^{+}	554 ± 13	2323 ± 332	7729 ± 2017	554 ± 20	11.10 ± 0.11	2.65 ± 0.06	1.54	1.47	4	B
15432	53.14614830	−27.77988200	2.640	...	482	48 ± 5	...	...	65 ± 12	10.85 ± 0.14	1.16 ± 0.01	1.47	1.16	4	B
10973	53.18582930	−27.80996560	2.583	4	593	47 ± 8	...	...	316 ± 17	10.76 ± 0.22	0.39 ± 0.02	0.99	1.27	4	B
7670	53.14817910	−27.83916220	2.150	...	...	110 ± 5	1755 ± 242	7616 ± 2650	115 ± 14	11.22 ± 0.11	2.87 ± 0.10	1.53	1.81	5	C
24367	53.14392700	−27.67773850	2.420	...	475	78 ± 8	$1290 \pm$	...	207 ± 16	11.20 ± 0.09	2.67 ± 0.13	1.56	1.74	5	B
18562	53.02739130	−27.75388610	2.040	...	...	67 ± 6	...	...	34 ± 9	11.28 ± 0.06	2.97 ± 0.09	1.91	1.64	5	B
14876	53.11879020	−27.78281820	2.309	1,2	...	207 ± 7	7068 ± 683	28531 ± 4479	365 ± 28	10.79 ± 0.05	1.83 ± 0.03	1.26	1.42	4	B
22883	53.14216250	−27.70742850	2.150	...	...	176 ± 9	...	...	75 ± 13	10.82 ± 0.33	1.77 ± 0.07	1.77	1.02	2	B
22200	53.05424860	−27.72164870	2.307	1	...	174 ± 8	1549 ± 245	8467 ± 2183	197 ± 11	11.06 ± 0.07	1.89 ± 0.05	1.64	1.68	5	B
21901	53.12859620	−27.72429960	2.020	...	...	91 ± 7	1278 ± 281	...	47 ± 16	11.28 ± 0.09	2.77 ± 0.10	1.80	1.70	5	B([O III])
26788	53.09951770	−27.70616110	2.260	...	...	179 ± 8	1094 ± 415	...	117 ± 9	11.08 ± 0.18	2.17 ± 0.08	1.37	1.52	4	B([O III])
7579	53.14454840	−27.83969560	2.050	...	...	128 ± 6	...	...	96 ± 7	11.14 ± 0.12	2.64 ± 0.07	1.51	1.46	4	B
15377	53.02228390	−27.77890030	2.650	...	111^{+}	178 ± 9	1531 ± 271	...	108 ± 14	11.10 ± 0.07	1.79 ± 0.10	1.63	1.22	2	...

Notes. Column 1: General ID in Guo et al. (2013). Columns 2 and 3: R.A. and declination J2000. Column 4: photometric or spectroscopic redshift. Column 5: spectroscopic redshift from different references: (1) Barro et al. (2014) (*Keck* MOSFIRE), (2) Kurk et al. (2013) [GMASS-2578,2443,2467,1989,2043], (3) Kriek et al. (2008), (4) Balestra et al. (2010), (5) Silverman et al. 2010, (6) Wuyts et al. (2009), (7) Vanzella et al. (2008), (8) D. Stern et al in preparation, (9) Szokoly et al. (2004). Column 6: X-ray ID in Xue et al. (2011). The superscript index indicate degree of contamination on the SED from AGN emission based on the comparison to SED-fits that include AGN templates (See Section 3.5). *+:* Severe. *-:* Mild. Columns 7–9: far-IR fluxes in *Spitzer*/MIPS 24 μm and *Herschel*/PACS 100 μm and SPIRE 250 μm. Column 10: total star formation rate ($\rm SFR_{UV+IR}$ [$M_{\odot}{\rm yr}^{-1}$]), see Section 2.2. Column 11: stellar mass ($\log(M/M_{\odot})$) determined from SED fitting using Bruzual & Charlot (2003), see Section 2.2. Column 12: circularized, effective (half-light) radius (kpc) measured with GALFIT, see Section 2.2. Columns 13 and 14: rest-frame colors estimated from the best-fit stellar template using *EAZY*. Column 15: location of the galaxy in the regions of the *UVJ* diagram indicated in Figure 2. Column 16: qualitative flag for the G141 spectra: (A) highest signal-to-noise spectra, showing a continuum break and (occasionally) absorption lines, or a emission line ([O II] or [O III]/Hβ, indicated); (B) low signal-to-noise, absent continuum break, weak emission lines; (C) significant flux contamination or truncated spectrum.

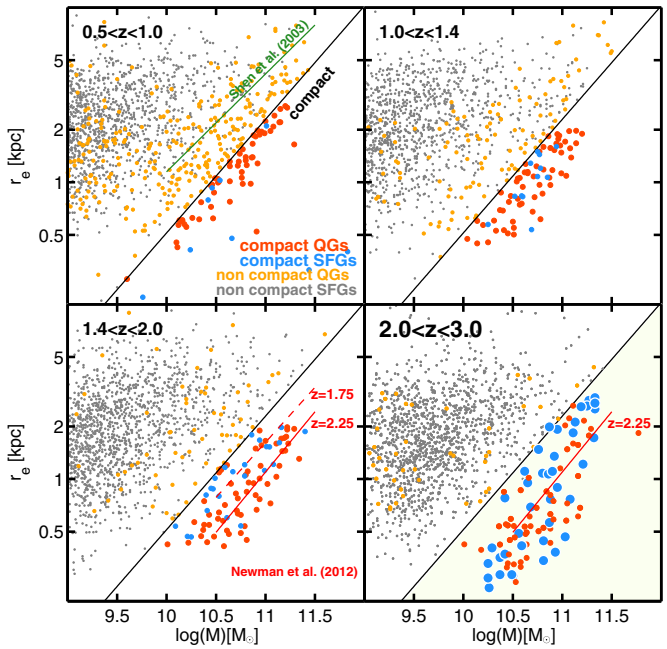

Figure 1. Evolution of the mass–size distribution from $z = 3$ to $z = 0.5$ for galaxies in GOODS-S. The black line shows the compactness selection criterion ($\Sigma_{1.5} = 10.3\,M_{\odot}$ kpc$^{-1.5}$). The colored markers indicate compact and noncompact SFGs (blue/gray) and quiescent galaxies (red/orange). The colored lines show the mass–size relation for quiescent galaxies at $z = 2.25$ and 1.75 (red) from Newman et al. (2012) and at $z = 0$ (green) from Shen et al. (2003). Note the steady increase in radii of these population with time. The 45 compact SFGs at $2 < z < 3$ (bottom-right panel) analyzed in this paper are highlighted with larger marker sizes. At $z \gtrsim 2$ the majority of compact galaxies (highlighted area below the black line) are star-forming, as opposed to lower redshifts where these are predominantly quiescent.

(A color version of this figure is available in the online journal.)

$0.5 < z < 3.0$. The subpopulations of compact SFGs and quiescent galaxies are highlighted in blue and red, respectively. As discussed in B13 and other previous works, the region limited by the $\Sigma_{1.5}$ threshold encloses most of the quiescent population at $z \gtrsim 1.4$, which appears to follow a very tight mass–size correlation with a nearly constant slope and an increasing zero point toward larger sizes as a function of time (see, e.g., Cassata et al. 2011; Newman et al. 2012). Interestingly, at $z \gtrsim 2$, this region becomes more densely populated with compact SFGs (large blue markers), which are not nearly as abundant at lower redshifts (Figure 2 of B13). The changing nature of the galaxies populating the compact region, from star-forming to quiescent around $z \sim 2$, jointly with the remarkable similarity of their structural properties (Sérsic, r_e and $\Sigma_{1.5}$) and the rapid increase in the number density of compact quiescent galaxies (Cassata et al. 2013), was interpreted in B13 as an indication of the evolutionary connection between the two populations.

2.4. 3D-HST NIR Grism Spectra of Compact SFGs

In order to improve the spectral characterization of the compact SFGs, we combined the broadband photometry SEDs with *HST*/WFC3 G141 grism spectroscopy from the 3D-HST survey (Brammer et al. 2012). The grism provides continuous wavelength coverage from $\lambda = 1.1$ to 1.6 μm with medium resolution ($R \sim 130$; 47 Å pixel^{-1}), yielding 5σ continuum detections for sources brighter than $H_{F140W} = 23$. This allows us to improve the spectral resolution around the age-sensitive features in the rest-frame optical of galaxies at $z \gtrsim 2$ ($\lambda_{\rm rest} \sim$ 4000 Å; e.g., Kriek et al. 2011; Whitaker et al. 2013). The source catalog and one-dimensional flux-calibrated spectra reduced with the aXe software (Kümmel et al. 2009) were drawn from Trump et al. (2013). All compact SFGs fall within the area covered by the G141 observations. However, the grism spectra of nearby objects can sometimes overlap with the main extraction, causing partial, or severe, flux contamination (Brammer et al. 2012). Nevertheless, the aXe reduction provides a contamination estimate that can be used to determine the uncontaminated spectral range. Based on that determination, we extracted good-quality spectra (<1% contamination) for 36 of the 45 compact SFGs.

Figure 2 illustrates the procedure to merge a G141 spectrum with the broadband SED. Briefly, we extract the one-dimensional spectrum in the wavelength range 1.1–1.7 μm at a native resolution of 46.5 Å pixel^{-1}. Then, we convolve it with a square filter transmission of FWHM = 200 Åfor the purpose of combining it with the broadband photometry. The spectra are already flux calibrated, but we perform an additional recalibration by comparing to the broadband photometry in F140W and F125W. This results in small variations of less than 2% level. For the faintest objects in the sample, we bin the spectra by a factor of 2−3 to increase the signal-to-noise ratio (S/N) at the expense of lowering the spectral resolution.

At $2 < z < 3$ the G141 spectra can yield detections of emission lines due to [O III] or [O II], or absorption lines in the Balmer series or the G band. However, due to the low spectral resolution and the additional broadening caused by the intrinsic galaxy shape, high equivalent width (EW) emission lines are more easily detected (e.g., Trump et al. 2011; Fumagalli et al. 2012) than absorption lines, which are only identified with high significance in bright galaxies (van Dokkum & Brammer 2010) or in stacked spectra (e.g., Whitaker et al. 2013; Bedregal et al. 2013; Krogager et al. 2013). Among our compact SFGs, only three galaxies show emission lines, and another six (with confirmed spectroscopic redshift) show evidence of absorption lines at the appropriate rest-frame wavelengths (Barro et al. 2014). Nonetheless, the grism data provide a solid detection of the stellar continuum (top-right panel of Figure 2), which, when combined with the broadband photometry, increases the spectral resolution of the SED, improving the quality of the photometric redshifts and the estimated stellar properties (Brammer et al. 2012; Bedregal et al. 2013). Roughly half of the members of the sample (23/45; see Table 1) have previous spectroscopic redshifts. For those galaxies, the overall accuracy of the photometric redshifts based on the composite SEDs is better than 1% ($\Delta z/(1+z) = 0.7\%$).

3. PROPERTIES OF COMPACT SFGs AT $2 < z < 3$

In this section we review and expand the analysis of the properties of compact SFGs at $2 < z < 3$ presented in B13, and in Sections 4 and 5 we model their stellar populations to verify whether the proposed evolutionary connection with compact quiescent galaxies is consistent with the estimated ages, quenching times, and evolutionary tracks on the SFR–M diagram.

3.1. Distribution in the SFR–M Plane

The left panel of Figure 3 shows SFR versus stellar mass for all SFGs (boxed gray scale) and quiescent galaxies (red markers) at $2 < z < 3$, highlighting the location of compact SFGs (blue markers; the shade of blue indicates the strength of the far-IR

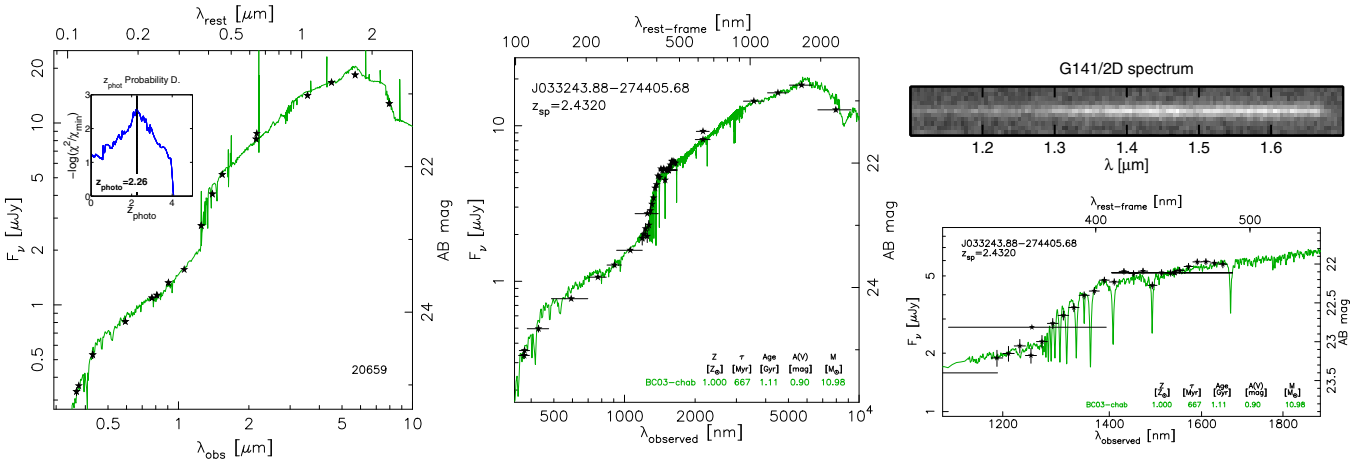

Figure 2. Description of the procedure to merge multiwavelength broadband photometry with G141 grism spectroscopy to create a composite SED. Left panel: best-fit stellar template to the broadband SED. The photometric redshift probability distribution (upper-left inset) and the best-fit value are indicated. Right panel: above, the 2D-G141 spectrum of the example galaxy. Below, the 1D spectrum collapsed in the spatial direction and divided in discrete photometric blocks created by convolving the data with square filters of FHWH = 200 Å. A small (<2%) correction is applied to the G141 flux calibration based on the comparison to F125W and F140W photometry (black stars). Central panel: best-fit stellar template to the merged broadband plus grism SED. The increased spectral resolution of the composite SED provides tighter constraints on the SED modeling, increasing the precision of photometric redshift and stellar population properties.

(A color version of this figure is available in the online journal.)

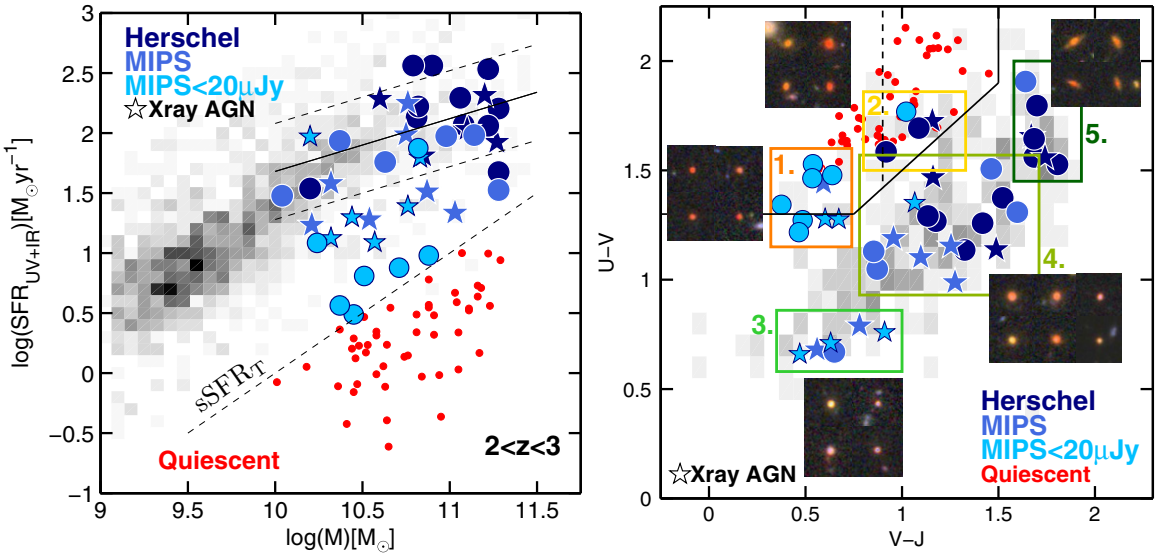

Figure 3. Left panel: SFR–mass diagram for all galaxies at $2 < z < 3$ in the parent catalog. The boxed gray scale shows the main sequence of SFGs. The red markers show the quiescent population ($\log(\mathrm{sSFR/Gyr^{-1}}) < -1$; dashed black line). Compact SFGs are shown in blue colors; cyan indicates galaxies undetected in the far-IR ($S_{24\,\mu m} < 20\,\mu$Jy); the other two (light to dark) colors indicate detections in *Spitzer*/MIPS 24 μm and *Herschel* (PACS or SPIRE). Far-IR emission is usually associated with a higher level of dust obscuration and SFR activity. The stars indicate that the galaxy hosts an AGN. The black line (dashed) shows the best fit ($\pm 3\sigma$) to the main sequence of massive ($\log(M/M_\odot) > 10$) SFGs. Only two compact SFGs present SFRs 3σ above the main sequence (*starburst* galaxies; Daddi et al. 2010). Right panel: *UVJ* diagram for galaxies more massive than $\log(M/M_\odot) > 10$ (boxed gray scale). The symbols indicate the same as in the left panel. For the purpose of further discussion, we divide the diagram into five regions (see, e.g., Figure 8). Regions 1 and 2 (orange/yellow) overlap partially with the *UVJ*-quiescent area, including mainly galaxies with lower SFRs. Regions 3–5 (green) contain SFGs with increasing levels of extinction and larger stellar masses from left to right. The $5'' \times 5''$ (ACS/WFC3) *zJH* color stamps show representative examples of galaxies in each region. Compact SFGs present undisturbed spheroidal morphologies, except the most obscured ones, which appear to be edge-on and disk-like.

(A color version of this figure is available in the online journal.)

detection). A correlation between SFR–M, usually referred to as the "main sequence" of SFGs (Noeske et al. 2007; Elbaz et al. 2011), is visible across the whole mass range. In agreement with previous studies of massive galaxies ($\log(M/M_\odot) > 10$), we find that the majority of compact SFGs present dust-obscured star formation (Papovich et al. 2007; Pérez-González et al. 2008b; Bauer et al. 2011), based on their detection at mid- to far-IR wavelengths: 71% are detected in MIPS 24 μm, and 44%/13% are detected in *Herschel* PACS/SPIRE, respectively. All *Herschel* detections are also recovered in the deeper 24 μm data ($S_{24\,\mu m;3\sigma}$ ~20μJy versus ~1 mJy in the *Herschel* bands). In addition, the fraction of IR detections increases toward the most massive galaxies, indicating that IR luminosity and in general dust attenuation ($A(V) \propto L_{IR}/L_{UV}$; Barro et al. 2011) both correlate with stellar mass in SFGs, i.e., the most massive SFGs are more obscured (Brammer et al. 2011; Wuyts et al. 2011b).

The fraction of compact SFGs among all massive SFGs is ~20%. This number, however, depends on the stellar mass, increasing from 10% to 30% and 37% at $\log(M/M_\odot) =$ [10–10.6], [10.6–11.2], and [>11.2]. This is because, at the

high-mass end, the number of noncompact SFGs and the scatter in their mass–size distribution (i.e., the range in $\Sigma_{1.5}$) decrease, leading to an increase in the relative number of compact versus extended SFGs (below and above the black line in Figure 1).

In agreement with previous works, we find a flattening in the slope of the main sequence at the high-mass end (Bauer et al. 2011; Whitaker et al. 2012b). The black line in Figure 3 shows the best fit ($\pm 3\sigma$) to a single power law ($\alpha = 0.44$) for all massive ($\log(M/M_{\odot}) > 10$) SFGs. With respect to this fit, most compact SFGs are found either on the main sequence (∼65%) or below it (∼30%), which is consistent with the idea that at least some of these galaxies are in transit to the red sequence. We note also that compact SFGs below the main sequence have a stellar mass distribution more skewed toward smaller values ($\log(M/M_{\odot}) = 10$–10.6) than those in the main sequence (see also Section 4.1.1 for further discussion). Only two compact SFGs present SFRs slightly above the 3σ upper limit of the main sequence (we reject another two due to AGN contamination; see next section). Such galaxies, usually called *starburst* (Daddi et al. 2010; Rodighiero et al. 2011), are thought to be in a short-lived, high star formation efficiency phase (high gas-to-star formation ratio), possibly triggered by an external mechanism, such as mergers or galaxy interactions. If compact SFGs are the precursors of the quiescent population, the small *starburst* fraction suggests that quenching is not usually preceded by a strong peak in the SFR, or, alternatively, the duty cycle of the *starburst* phase is very short compared to the duration of the star-forming phase. Incidentally, we do not find evidence for tidal features or disturbed appearances in either of these two galaxies, but we note that these are not necessarily representative of the whole *starburst* population, as is the case in, e.g., Kartaltepe et al. (2012).

3.2. Extinction Properties

The right panel of Figure 3 shows the rest-frame $U-V$ versus $V-J$ color (hereafter *UVJ*) for compact SFGs and other massive star-forming and quiescent galaxies at $2 < z < 3$. The *UVJ* diagram is an alternative diagnostic to distinguish between reddened star-forming and quiescent galaxies according to their SEDs. This method has been shown to be very successful in breaking the dust/age degeneracy using the $V-J$ color as a proxy for dust attenuation (Wuyts et al. 2007; Williams et al. 2010; Whitaker et al. 2011). The *UVJ* colors of compact SFGs are consistent with their distribution on the SFR–M diagram and support the idea of their transitory nature from star-forming to quiescent. Roughly 70% of the compact SFGs, predominantly those with far-IR detections, present red $V-J$ colors characteristic of dusty SFGs, while the remaining ∼30% appear to lie within (or close to) the quiescent region. Within the latter, we also find evidence for differences in the attenuation level as a function of the $V-J$ color. Those with lower extinctions, to the left of $\sim V-J = 0.75$, were identified in Whitaker et al. (2011) as recently quenched galaxies, following a nearly vertical color track (i.e., maintaining a low extinction) starting as low-mass, unextinguished galaxies. If that is the case, those nearly quiescent galaxies at $V-J = 0.75$ could indicate the arrival point on the red sequence for more dusty compact SFGs. We further investigate the possible evolutionary tracks of compact SFGs in the *UVJ* diagram as a function of their stellar mass and SFH in Section 5.2. For the purpose of further discussion in the following sections, we divide the *UVJ* diagram into five regions, roughly corresponding to the following overall properties: (1) low SFR, low extinction; (2) low SFR, higher extinction; (3, 4, and 5) star-forming with increasing stellar mass and extinction.

3.3. Structural Properties and Visual Appearance

Compact SFGs are selected to have high stellar mass surface densities similar to those of quiescent galaxies at $z \sim 2$. This means that, for a given slice in stellar mass, compact SFGs exhibit the remarkably small effective radii of quiescent galaxies while having the SFRs of normal, main-sequence galaxies (Figure 4). As a result, they occupy a distinct region in the specific star formation rate (sSFR)–Σ diagram, which, combined with the lack of extended-quiescent galaxies, suggests that, at these redshifts, the quenching of star formation takes place in the most compact (higher $\Sigma_{1.5}$) galaxies (see, e.g., Cheung et al. 2012 and Fang et al. 2013 for an extension of this result to lower redshifts), and thus compact SFGs are the immediate progenitors of the quiescent population. Under the assumption that galaxies grow in both stellar mass and size during their star-forming phase, the natural precursors of massive, compact SFGs are larger SFGs, suggesting that the evolutionary sequence in Figure 4 goes from extended to compact SFGs (left to right) and then to quiescence by simply shutting down star formation. This sequence implies also the need for a mechanism to shrink the size and to change the structure of extended SFGs, transforming them into compact SFGs. We explore these mechanisms in Section 6.

The evolution from compact SFGs to compact quiescent galaxies is supported by the histograms in Figure 5, which show that compact SFGs span roughly the same range in stellar mass ($\log(M/M_{\odot}) = 10$–11.5) as quiescent galaxies, while having high Sérsic indices ($n = 3.4$) and axis ratios ($b/a = 0.75$), characteristic of that population (e.g., Szomoru et al. 2012; Bell et al. 2012). A two-sample Kolmogorov–Smirnov test yields a statistic $S = 0.12$, 0.18, and 0.22 with a p-value of 99.9%, 98.5%, and 96.7% for stellar masses, axis ratio, and Sérsic indices, respectively, and it is thus not inconsistent with the two distributions being drawn from the same parent distribution. We also find a trend with stellar mass such that the most massive ($\log(M/M_{\odot}) > 11$) and larger ($r_e > 2$ kpc) compact SFGs are more akin to edge-on disks, with lower Sérsic indices and a flatter distribution of axis ratios (dark-blue line in Figure 5). This, however, is also true for massive compact quiescent galaxies at $z \sim 2$ (van der Wel et al. 2011; Bruce et al. 2012; Chang et al. 2013), indicating that the structural similarities between the two populations are also preserved at different stellar masses. The black dash-dotted line in Figure 5 shows the distribution of Sérsic values for X-ray-detected compact SFGs, which appears to be consistent with that of the other compact SFGs. Thus, we do not find evidence for contamination in the structural properties of the galaxies as a result of having a bright point source at the center of an otherwise smooth light profile.

In terms of their visual appearance, compact SFGs show undisturbed spheroidal morphologies, very similar to compact quiescent galaxies, but strikingly different from noncompact SFGs, which are predominantly disk-like or irregular (right panel of Figure 4). Only the most massive and dust-obscured galaxies, mainly in region 5 of the *UVJ* diagram, present different morphologies, more similar to edge-on disks or patchy galaxies with diffuse light profiles nearly undetected in the rest-frame UV images (see also Patel et al. 2012). Indeed, their selection as compact galaxies may be partially due to an inclination effect. Signatures of mergers or interactions are uncommon among compact SFGs and, in general, among

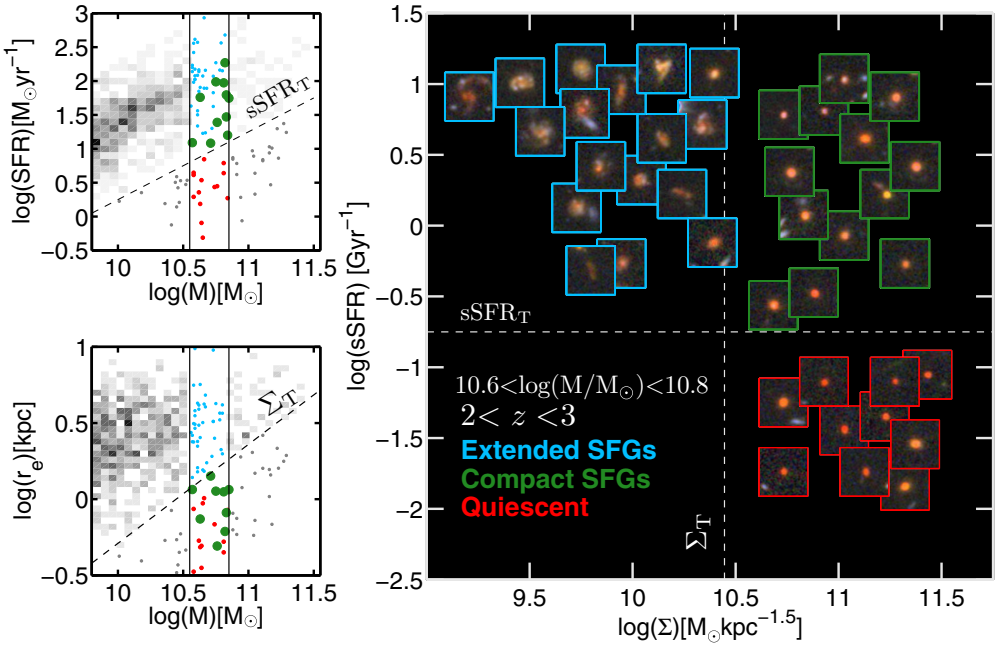

Figure 4. Left panels: distribution of galaxies at $2 < z < 3$ (boxed gray scale) in the SFR–M (upper panel) and M–size (lower panel) diagrams. The colored markers indicate compact SFGs (green), other noncompact SFGs (cyan), and quiescent galaxies (red) in a thin slice of stellar mass ($10.6 < \log(M/M_\odot) < 10.8$; vertical black lines). The dashed lines show the selection thresholds for star-forming (above $\log(\mathrm{sSFR/Gyr^{-1}}) = -1$) and compact (below $\log(\Sigma_T/M_\odot\,\mathrm{kpc}^{1.5} = 10.3$) galaxies. Compact SFGs have nearly *normal*, main-sequence SFRs, but small effective radii typical of the quiescent population. Right panel: sSFR–Σ diagram showing the galaxies in the highlighted mass slice of the left panels. The location of compact SFGs in the upper-right quadrant and the lack of galaxies in the lower-left quadrant suggest that the formation of compact quiescent galaxies follows an evolutionary sequence from extended (upper left) to compact (upper right) SFGs, likely due to a strongly dissipational process (see Section 6), and then to quiescence (bottom right) by simply shutting down SFR. The $5'' \times 5''$ *zJH* color postages illustrate that compact SFGs not only share the stellar masses and effective radii of quiescent galaxies but also present similar spheroidal morphologies, significantly different from those of extended SFGs, which appear to be disk-like and sometimes irregular or clumpy.

(A color version of this figure is available in the online journal.)

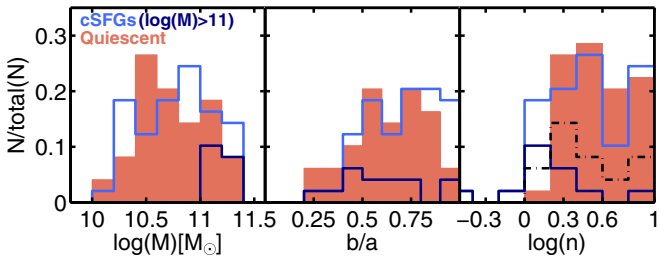

Figure 5. Left to right panels: distribution of stellar masses, axis ratios, and Sérsic indices for compact SFGs (light blue) and quiescent galaxies (red). Both populations have consistent stellar mass distributions and similarly high values of the axis ratio and the Sérsic index, typical of a spheroid-dominated population. The dark blue line indicates the distribution of the most massive ($\log(M/M_\odot) > 11$) and larger ($r_e > 2$ kpc) compact SFGs, which appear to have more disk-like morphologies and a flatter distribution of axis ratios. The black dashed-dotted line shows the Sérsic index distribution for X-ray-detected compact SFGs, which is fully consistent with that of the full compact SFG population, i.e., there is no evidence for a systematic bias in their structural properties.

(A color version of this figure is available in the online journal.)

spheroidal galaxies at $z \sim 2$ (Kaviraj et al. 2013a). The few examples of disturbed morphologies within our sample appear to be in the most unobscured galaxies in region 3 of the *UVJ* diagram. Interestingly, three of these galaxies host the most luminous X-ray galaxies ($L_X > 10^{44}$ erg s^{-1}) in the sample.

3.4. Far-IR Colors and SEDs

The emission at mid- to far-IR wavelengths is typically associated with dust heated by star formation. However, if part of this emission originates from a different source, such as an AGN or an evolved stellar population, it could lead us to overestimate the IR-based SFR. The latter case appears to be relevant only for galaxies with low SFRs (Salim et al. 2009; Fumagalli et al. 2013); however, an obscured AGN can have a significant contribution to the IR emission even in strongly SFGs (Daddi et al. 2007a, 2007b). The shape of the IR SED, probed by *Spitzer*/*Herschel* colors, provides an effective diagnostic tool to identify the power source of the dust heating (e.g., Kirkpatrick et al. 2013). Dust heated by star formation has colder temperatures ($T_{\rm dust} = 15$–50 K) and thus emits at longer wavelengths than dust heated by an AGN ($T_{\rm dust} = 150$ K), which is a more intense heating source. Figure 6 shows the S_{250}/S_{24} and S_{100}/S_{24} *Spitzer*/*Herschel* colors versus the $S_{8.0}/S_{3.6}$ IRAC color for 19 (7) compact SFGs detected in PACS (SPIRE) compared with other massive SFGs at $2 < z < 3$. In the presence of an AGN, the emission at shorter wavelengths leads to bluer *Herschel* colors and redder IRAC colors, typically within the gray shaded areas. IRAC colors have been widely used in the literature as an AGN selection criterion (e.g., Lacy et al. 2004; Stern et al. 2005; Donley et al. 2007) but, combined with their *Herschel* colors, also provide additional information on the heating source (star formation versus AGN) or the nature of the star formation (main sequence versus starburst). To illustrate these differences, Figure 6 shows color tracks of IR templates with increasing levels of AGN activity (purple) and IR luminosity (red).

The overall *Herschel* colors and the distribution with respect to other SFGs indicates that the IR emission in compact SFGs is mainly fueled by star formation. Only two out of six

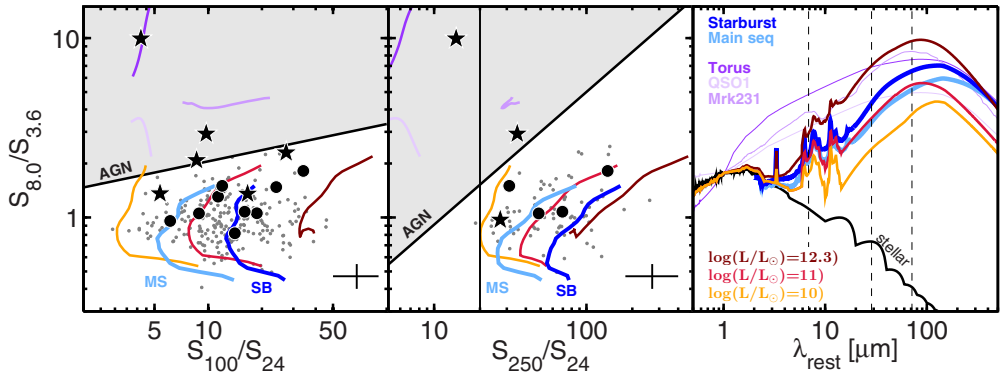

Figure 6. Far-IR (*Spitzer*/*Herschel*) color–color diagrams for compact (black) and noncompact (gray) SFGs at $2 < z < 3$ detected in PACS 100 μm (left panel) and SPIRE 250 μm (central panel). Stars indicate X-ray detections. The gray shaded area indicates the selection region for galaxies with a significant AGN contribution to the IR emission (Kirkpatrick et al. 2013). Also from Kirkpatrick et al. (2013), the vertical line at $S_{250}/S_{24} = 30$ indicates the minimum color for a typical star-forming SED. Galaxies to the right of that line are expected to have significant star formation regardless of their AGN emission. The solid lines indicate evolutionary tracks (bottom to top from $z = 2$ to 3) for three groups of IR SEDs shown in the right panel, namely, AGN dominated (purple), SFGs with increasing L_{TIR} (orange to brown) drawn from the library of Chary & Elbaz (2001), and the *main-sequence*/*starburst* templates of Elbaz et al. (2011). The dashed lines in the right panel indicate rest-frame wavelength probed by MIPS 24 μm, PACS 100 μm, and SPIRE 250 μm for a galaxy at $z = 2.5$. Overall, compact SFGs present colors consistent with star formation and IR SEDs ranging between the *main-sequence* and *starburst* templates. Only three X-ray-detected AGNs appear to have some AGN contribution to their IR SEDs. These galaxies are also flagged as AGN dominated based on their optical/NIR SEDs (Appendix A).

(A color version of this figure is available in the online journal.)

X-ray-detected compact SFGs (22603 and 9834) appear to have a significant contribution from the AGN to the IR emission, whereas the other four present colors consistent with, or slightly above, the star-forming range. The first two galaxies and another one of the second group were already excluded from our analysis on the basis of AGN contamination in the stellar SED, but they are shown in this section to illustrate the effects of AGN emission in the IR colors.

We also find an excellent agreement between the main-sequence/*starburst* classification derived from the SFR–M diagram and the *Herschel* colors. Only two galaxies (25998 and 14876), the same ones above the main sequence in Figure 3, appear to have a high $S_{100}/S_{24} > 20$ ratio characteristic of *starburst* galaxies. The remaining compact SFGs lie roughly between the tracks of the main-sequence and *starburst* templates (Elbaz et al. 2011; Magdis et al. 2012), with IR luminosities in the range $L_{TIR} = 10^{10.8-11.6}\,L_{\odot}$.

3.5. AGN Identification from X-Rays

Using the *Chandra* 4 Ms catalog, we find that roughly ∼20% of all massive ($M_{\star} > 10^{10}\,M_{\odot}$) galaxies at $2 < z < 3$ host an X-ray-detected AGN (see also Wang et al. 2012). Interestingly, the majority of these luminous ($L_X > 10^{43}$ erg s^{-1}) AGNs are found in compact hosts. In this sample, which covers a slightly wider area of GOODS-S than B13, 47% (21/45) of the compact SFGs are X-ray-detected AGNs, six of which are also selected using the IRAC power-law criteria (Donley et al. 2007, 2008; Caputi 2013). Note also that, at the depth of the 4 Ms *Chandra* survey, only the most luminous AGNs can be detected at $z > 2$. Thus, the intrinsic fraction could be higher if we were able to detect lower-luminosity AGNs. For comparison, only 9% and 17% of the noncompact SFGs and compact quiescent galaxies host an AGN. In the context of the evolutionary sequence, the large fraction of AGNs among compact SFGs suggests that the transformation from extended to centrally concentrated compact SFGs triggers a phase of black hole and stellar bulge growth that could signal the building of the $M_{\star} - \sigma$ relation (Cisternas et al. 2011; Mullaney et al. 2012).

Compact SFGs with and without AGNs (stars in Figure 3) appear to have a similar distribution in the *UVJ* and SFR–M diagrams, which provides no conclusive evidence on the role of the AGN in the quenching of the star formation. We note, however, that the high AGN fraction among compact SFGs makes the quenching scenario more likely at high redshift than in the local universe, where AGNs are more frequent among older SFGs or post-starburst galaxies (Davies et al. 2007; Wild et al. 2010; Yesuf et al. 2013).

4. STELLAR POPULATION MODELING OF COMPACT SFGs

In Section 2.4 we described the method to create composite SEDs combining broadband photometry in 17 bands with WFC3/G141 grism spectroscopy. Here we make use of these detailed SEDs to estimate the stellar properties of compact SFGs from SED fitting. In particular, we focus on deriving stellar ages and formation timescales (see also Appendix B for a discussion on SFRs), and we study the differences arising from the use of three different parameterizations of the SFH, namely, single (Section 4.1) and delayed (Section 4.2) exponentially declining (τ) models, and a library of SFHs derived from SAMs of galaxy formation (Section 4.3). There are different possible definitions of galaxy age that are frequently used in the literature (e.g., SFR- or mass-weighted ages; Wuyts et al. 2011a). Here we refer to the best-fit age as the time since the onset of star formation, $t = t_{obs} - t_{form}$.

4.1. Single τ Models

The main modeling assumptions used with single (and also delayed) τ models are the BC03 stellar library, a Chabrier (2003) IMF ($M \in [0.1\text{–}100]M_{\odot}$), with a Calzetti et al. (2000) attenuation law in the range $A_V = 0$–4, and solar metallicity. In addition, the e-folding times are required to be larger than 300 Myr to obtain a better agreement between the SFR_{IR+UV} and the best-fit SFR from the models (see Appendix A for detailed discussion). No other constraints are imposed on the best-fit ages.

The best-fit ages estimated from single τ models are in the range $t = 0.3$–1.1 Gyr, with a median value of $t = 850$ Myr. Based on those ages, the formation redshifts range between

$z_{\rm form} = 3.5$ and $z_{\rm form} = 4.2$. The majority of compact SFGs present best-fit *e*-folding times close to the minimum threshold, with a median value of $\tau = 400$ Myr and 90% of the galaxies presenting values lower than $\tau = 800$ Myr. The distribution of t/τ values peaks around ~2.6, as expected from the star-forming nature of the sample. For comparison, quiescent galaxies are often selected with a threshold of $t/\tau > 6$ (e.g., Fontana et al. 2009), which roughly corresponds to $\log({\rm sSFR/Gyr^{-1}}) = -1.5$.

4.1.1. Short-lived Compact SFGs

We verify that the overall χ^2 for constrained ($\tau > 300$ Myr) SED fits is fully consistent with the values obtained imposing no restrictions on the *e*-folding time. For the majority of galaxies a weak constraint favors solutions with smaller τ and younger ages for similar values of $\log(t/\tau) \sim$ constant, i.e., within the well-known degeneracy in age–τ (see, e.g., Figure 11 of Pérez-González et al. 2013).

Nevertheless, for the (low-sSFR) galaxies in region 1 of the *UVJ* diagram (Figure 3(b)) the constrained τ models overestimate the rest-frame UV luminosity ($\lambda_{\rm rest} < 3000$ Å), providing a poor fit in that spectral range. Forcing a maximally old age to reduce the UV luminosity worsens the χ^2, suggesting that shorter formation timescales (i.e., shorter τ) are required to reproduce the SEDs of these galaxies. Indeed, the unconstrained τ models provide the best fit for typical *e*-folding times of $\tau = 10$–30 Myr and a median age of $t \sim 1$ Gyr. As mentioned in Section 3.2, region 1 of Figure 3(b) was identified in Whitaker et al. (2012a) as the arrival point on the red sequence for recently quenched galaxies (see also McIntosh et al. 2014). The small values of τ needed to fit these galaxies suggest that this is not only the arrival point for recently quenched galaxies, but specifically for galaxies with short assembly histories, i.e., a "fast track" to the red sequence. Meanwhile, other compact SFGs, well reproduced with constrained τ models, may follow a different route to the quiescent region of the *UVJ*. We further discuss this possibility in Sections 4.3 and 5.2.

4.2. Delayed τ Models

Several recent papers have addressed the issue of how the use of different SFHs affects the best-fit stellar properties (Lee et al. 2009; Pforr et al. 2012). While it is not yet clear what is the preferred functional form, there is a general agreement on the limitations of declining τ models to recover the stellar properties of young SFGs at $z \gtrsim 3$ (Finlator et al. 2011; Papovich et al. 2011; Schaerer et al. 2011). The problem arises because some galaxies might undergo increasing, rather than decreasing, SFHs during the early phases of their lives. For such galaxies there is often a better agreement between the properties derived from SED modeling and observed estimates of the stellar age and SFR using *inverted* (exponentially increasing) τ models or the delayed models, ${\rm SFR} \sim t \times \exp(-t/\tau)$ (Maraston et al. 2010; González et al. 2014; Curtis-Lake et al. 2012). The main difference between single and delayed τ models is an early phase ($t \ll \tau$) of increasing SFR in the latter, while at intermediate to late times both models present the same exponential decline with time (Figure 7).

We find, however, that none of the compact SFGs are in the increasing SFR phase at the epoch of observation, i.e., they are predominantly in intermediate to late evolutionary stages ($t > \tau$), for which the single and delayed τ models have similar behavior, and thus provide similar best-fit stellar properties. The only significant difference is that stellar ages are ~30% older in the delayed models, with values in the range $t = 0.5$–1.3 Gyr and a median value of $t = 1.1$ Gyr. The median *e*-folding time is the same in both models, $\tau = 400$ Myr, and the distribution is similarly skewed toward the minimum threshold, with 90% of the galaxies having $\tau < 1$ Gyr. The stellar masses are also fully consistent, with only a small offset ($\Delta\log(M/M_\odot) = 0.05$ dex) toward larger stellar masses in the delayed models. The typical scatter of the comparison is smaller than 0.1 dex. Thus, we conclude that, for compact SFGs, the use of single or delayed τ models produces similar best-fit results, with the only noticeable difference of slightly older stellar ages in the latter.

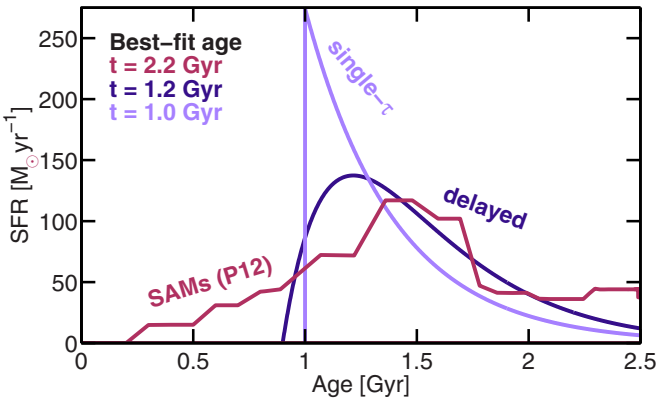

Figure 7. Example of the three different SFHs used to model the stellar populations of compact SFGs. The purple lines show the evolution of single and delayed τ models with the same $\tau = 300$ Myr. The main difference between them is an early phase ($t \ll \tau$) of increasing SFR in the latter. The magenta line illustrates a nonparametric SFH drawn from an SAM (Pacifici et al. 2012). SAM SFHs present fluctuations of the SFR on short timescales inherited from the accretion and merging histories of the SAMs. Due to having a gradual increase of the SFR at early times, SAM SFHs estimate older stellar ages than τ models.

(A color version of this figure is available in the online journal.)

4.3. SFHs from Semianalytic Models of Galaxy Formation

An alternative option to parametric SFHs is to use a library of physically motivated SFHs drawn from theoretical models of galaxy formation. The advantage of this approach is that the range of possible SFHs is more diverse, including increasing and decreasing phases, as well as sudden bursts of star formation caused by galaxy interactions. This method has been successfully used in Finlator et al. (2007) to analyze a sample of $z \sim 3$ galaxies using hydrodynamic simulations and, recently, in Pacifici et al. (2012, hereafter P12) to reproduce evolutionary paths of low- and high-mass galaxies at $z = 0$–1 using a template library derived from SAMs of a dark matter simulation (see also Tonini et al. 2012 for a similar analysis of brightest cluster galaxies). In this section we follow the latter approach to analyze the SFH of compact SFGs.

The details of the modeling procedure are described in P12. Briefly, the likelihood that each model in the template library reproduces the observed SED is computed using a Bayesian method. The best-fit value is determined from the minimum χ^2, and estimated properties are derived from the median of the probability density functions. The template library, consisting of 100,000 templates, is based on SFHs and chemical enrichment histories for galaxies drawn from the Millennium cosmological simulation (Springel et al. 2005) as processed by the semianalytical recipes of De Lucia & Blaizot (2007). The large-scale cosmological simulation follows the growth, interaction, and merging history of dark matter halos from redshift $z = 127$ to the present time, while the semianalytic

recipes of De Lucia & Blaizot (2007, see also Croton et al. 2006)) follow star formation and the associated metal production by gas falling into these dark matter halos. The star formation is controlled by the gas surface density following the Kennicutt (1998) relation, and it also depends on AGN and supernova feedback modeled after the prescriptions of De Lucia et al. (2004) and Kauffmann & Haehnelt (2000), respectively. The initial library is expanded in two ways: resampling galaxies at randomly drawn stages of their evolution (i.e., not only at the default redshift given by the model), and varying the sSFR and metallicity of each galaxy in the last 10 Myr (defined as *current* sSFR in P12) before the time of observation. The effect of these variations is similar to the addition of a recent burst or a sudden truncation of the SFR. The stellar populations are modeled using the latest version of the Bruzual & Charlot (2003) models with a Chabrier (2003) IMF and the two-phase dust attenuation recipe (birth clouds and ambient interstellar medium) of Charlot & Fall (2000).

In the next section we also make use of another library of SAM SFHs from Lee & Yi (2013). These SAMs follow a different dark matter halo merger tree drawn from a smaller *N*-body simulation (512^3 versus 10^{10} particles in Millennium) based on the Gatget-2 (Springel et al. 2005) and HaloFinder (Tweed et al. 2009) codes. In this model, star formation can happen either in a quiescent mode, in which cold gas turns into disk stellar components via gas contraction on a disk (Kauffmann et al. 1993), or in a burst mode, which is induced by galaxy mergers (Cox et al. 2008). The metallicity is kept fixed at subsolar and solar metallicities for hot and cold gas, respectively, and AGN and supernova feedback is modeled following the methods of Somerville et al. (2008) and Kauffmann & Haehnelt (2000).

We note that the only purpose of the Lee & Yi (2013) SAMs is to provide an auxiliary sample from which we could easily select a subset of simulated galaxies verifying the requirement of being quiescent (sSFR $< -1\,\mathrm{Gyr}^{-1}$) at $z \sim 2$. Thus, our main results in Section 4 are based on the full library from P12, which provides a more exhaustive coverage of the parameter space due to the improvements described above (see also Section 3.1 of P12). In Section 5 we use only 1630 templates, resampled 20 times, in the Lee & Yi (2013) library for comparison purposes.

4.3.1. Overall Results for SAM SFHs

On average, we find that the evolution of the best-fit SAM SFHs for compact SFGs is similar to that of a delayed τ model with a long *e*-folding time, particularly at mid- and late times (Figure 7). The key difference is that SAM SFHs present more gradual increase of the SFR during the rising phase at the onset of star formation. As a result, the best-fit stellar ages tend to be older than those of the τ models. The typical stellar ages for compact SFGs obtained with SAM SFHs range between $t = 1.6$ and 2.4Gyr, with a median value of $t = 2$ Gyr. This is a factor of $\sim$2 older than the estimates of the τ models. Attending to these values, their formation redshifts would increase from $z_{\rm form} = 3$–4 in the τ models to $z_{\rm form} = 6$–7, suggesting that these galaxies are nearly maximally old. The age of the universe at $z \sim 2.5$ is 2.6 Gyr. Despite the longer duration of the increasing SFR phase in SAM SFHs, we again find very few galaxies (<2%) with rising SFRs at the epoch of observation. The majority of compact SFGs present, on average, either declining or roughly constant SFRs.

Figure 8 shows the averaged best-fit SFHs for compact SFGs in different regions of the *UVJ* diagram from Figure 3(b). In Section 4.1.1 we showed that fits of the SEDs of (low-sSFR) galaxies in region 1 with τ models required short formation timescales ($\tau < 300$ Myr). The best-fit SAM SFHs support this result by showing that these galaxies have, on average, a bell-shaped SFH with an FHWM of only $\sim$500 Myr (shaded orange area). The average SFHs of compact SFGs in other regions show longer duration. As a result, galaxies in region 1 are also younger ($1.8^{+0.1}_{-0.2}$ Gyr) than the average of other compact SFGs ($2.2^{+0.1}_{-0.3}$ Gyr). The uncertainties in the median values reflect the intrinsic scatter in the SFHs of the galaxies in a given *UVJ* region. Regardless of this variance, all galaxies in Region 1 are preferentially fit by shorter SFHs, as shown in Figure 8 (orange line).

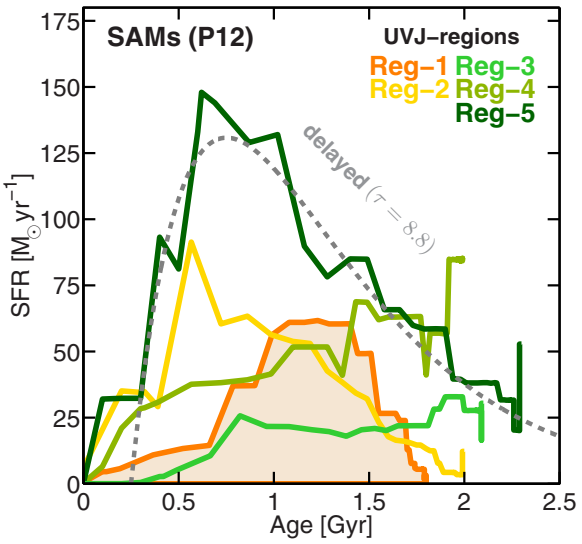

Figure 8. Averaged SAM SFHs for compact SFGs in different regions of the *UVJ* diagram. The colors indicate the regions in Figure 3(b). Galaxies in region 1 (orange shaded area) appear to have the shorter formation timescales, i.e., they assembled the bulk of their stellar mass in a shorter period of time. Galaxies in region 5 show an SFH similar to a delayed model with $\tau = 600$ Myr (dashed gray line). However, the majority of compact SFGs (regions 1, 3, 4) have a more gradual increase of the SFR at early times and a longer plateau phase (SFR$\sim$constant) than the delayed models.

(A color version of this figure is available in the online journal.)

The fact that younger compact SFGs have lower sSFRs than the older ones (see also Figure 11) implies that, in this case, age correlates with sSFR, contrary to intuition. We note, however, that such correlations only apply when using constant or declining SFHs, and when comparing galaxies with the same formation timescale (τ). Figure 8 also illustrates that, although some SAM SFHs may resemble the evolution of a long-τ delayed model, in general, they display a broad range of trends in SFR versus time, presenting phases of increasing, nearly constant, or rapidly decreasing SFR.

4.4. Summary of SFHs for Compact SFGs

We study the stellar populations of compact SFGs using two sets of SFHs: (1) exponentially declining (single and delayed) τ models, and (2) a library of physically motivated SFHs extracted from SAMs.

While both sets of SFHs produce similarly good fits to the SED in terms of reduced χ^2 and statistical errors for the inferred stellar properties, they differ in their quantitative predictions. SAM SFHs predict longer formation timescales and older ages, $t = 2^{+0.4}_{-0.2}$ Gyr ($z_{\rm form} = 6$–7), which are nearly a factor of two older than the estimates of single, $t = 0.9^{+0.2}_{-0.5}$ Gyr, and delayed, $t = 1.1^{+0.2}_{-0.6}$ Gyr, τ models ($z_{\rm form} = 3$–4). Such extreme

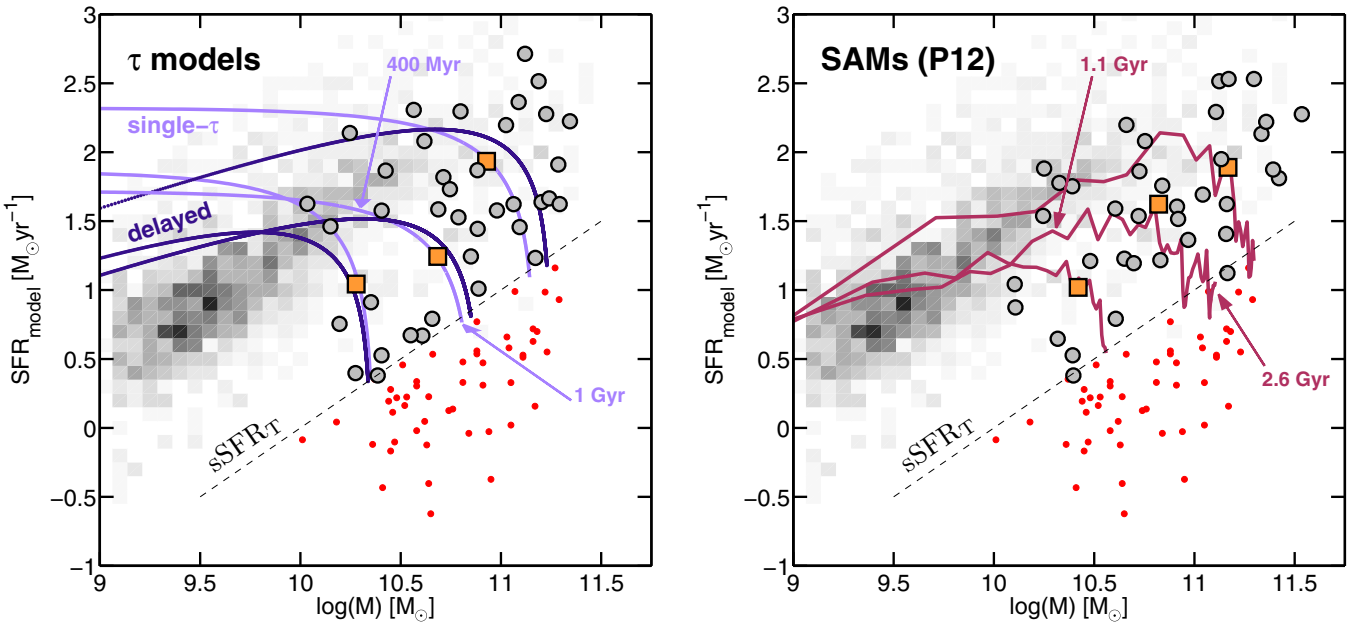

Figure 9. Distribution of the compact SFGs in the SFR–M diagram (gray circles) determined from the best-fit stellar masses and SFRs to single τ models (left panel) and SAM SFHs (right panel). The distribution of other (noncompact) SFGs (boxed gray scale) and quiescent galaxies (red) at $2 < z < 3$ is the same as in Figure 3. The purple lines in the left panel show the evolutionary tracks for three compact SFGs (orange squares) based on the best-fit SFHs to single and delayed τ models. In both cases, the slopes of the tracks appear to be shallower than the observed main sequence. The magenta lines in the right panel show the evolutionary tracks for the same three galaxies based on SAM SFHs. Qualitatively, these tracks are similar to those of the delayed models. However, the SAM tracks present a steeper slope closer to that of the main sequence and thus predict a longer duration of the star-forming phase. The best-fit stellar ages to SAM SFHs are also $\times 2$ older than in the τ models. This indicates that galaxies in the SAM tracks evolve at a slower pace than in τ tracks, as indicated by the time steps (arrows) in the left and right panels (see also Figure 11).

(A color version of this figure is available in the online journal.)

differences are a reflection of the systematics uncertainties associated with the SFH.

Even from the increased spectral resolution SEDs from *HST*/G141 data combined with broadband multi-wavelength photometry, we are not able to resolve spectral features that would conclusively distinguish between different SFHs. Sensitive indicators of the burstiness of the SFH, or the strength of a recent burst of star formation, such as the EW of Hα or the presence of strong Balmer lines in absorption, have been measured in stacks of galaxies with similar properties (Kriek et al. 2011; Whitaker et al. 2013; Bedregal et al. 2013), but either deeper grism observations or alternative spectroscopy would be required to perform similar measurements on individual galaxies.

In the next section we place additional constraints on the most likely SFHs for compact SFGs analyzing the impact of assuming different SFHs on (1) the shape of their evolutionary tracks in the SFR–M diagram and (2) the quenching time or the duration of the main sequence.

5. EVOLUTIONARY TRACKS OF COMPACT SFGs: LINKING PROGENITORS TO THEIR DESCENDANTS

In this section we study the evolutionary tracks of compact SFGs in the SFR–M and UVJ diagrams as inferred from their best-fit SFHs. In particular, we study the predictions of three different SFH models for the slope of the SFR–M correlation at early times ($t \ll t_{\rm obs}$) and the duration of the main-sequence phase for the compact SFGs. Then, we compare the galaxy number densities estimated from the forward extrapolation of these SFHs with the observed number density of quiescent galaxies and thus verify the proposed evolutionary sequence between the two populations. Finally, we study the distribution of compact SFGs in the UVJ diagram as a function of stellar mass and extinction, and we discuss the implications for their formation timescales and their history of dust production and destruction.

5.1. Evolutionary Tracks in the SFR–M Diagram

5.1.1. Early Growth and Duration of the Main Sequence

The left panel of Figure 9 shows the distribution of compact SFGs in the SFR–M diagram based on SFRs and stellar masses (gray circles) derived from single τ models. The values derived from delayed models are very similar and thus are not shown. However, the predicted evolution on the diagram is not the same for each model. The light and dark blue lines illustrate the differences in the evolutionary tracks (from the onset of star formation until they become quiescent) of three compact SFGs fitted with single and delayed τ models, respectively. While both models present the same exponential decline of the SFR at late ($t \gg t_{\rm obs}$) times, the predicted slope of the SFR–M correlation at early times ($t \ll t_{\rm obs}$) is different. For delayed models, the slope, $\log({\rm SFR}) = \alpha \log(M)$, is $\alpha \sim 0.50$, whereas for single τ models the SFR is nearly independent of the stellar mass, $\alpha \sim 0$. Neither of these, however, appears to follow the steeper observed slope of the main sequence at $z \gtrsim 2$ and $\log(M/M_\odot) < 10$ ($\alpha \sim 0.6$–1; e.g., Santini et al. 2009; Whitaker et al. 2012b), suggesting that these SFHs do not adequately reproduce the early phases of galaxy growth. If the SFR zero point of the main sequence keeps increasing at $z > 2$, it could explain a flatter slope for an evolutionary track that follows the main sequence as a function of time. However, the evolution of the SFR zero point since $z \sim 4$ to $z \sim 2$ is not strong enough to reproduce the flat evolutionary track of the single τ models (ΔsSFR ~ -0.2 dex; Stark et al. 2009; Karim et al. 2011; Bouwens et al. 2012; González et al. 2014).

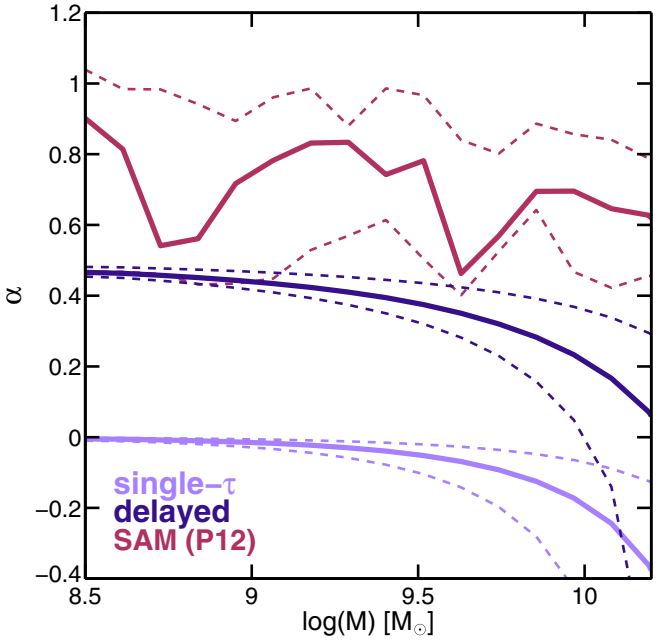

Figure 10. Average slope, α, of the evolutionary tracks in the SFR–M diagram for all compact SFGs (Figure 9 illustrates those tracks for three galaxies). The colors indicate the different SFH models used in the SED fitting. The solid and dashed lines show the median and 1σ upper and lower limits of the distribution, respectively. Overall, SAM SFHs present a steeper slope, $\alpha \sim 0.6$, closer to the observed value for the loci of the main sequence at $\log(M/M_{\odot}) \gtrsim 10$, $\alpha \sim 0.6$–1 (e.g., Rodighiero et al. 2011; Whitaker et al. 2012a).

(A color version of this figure is available in the online journal.)

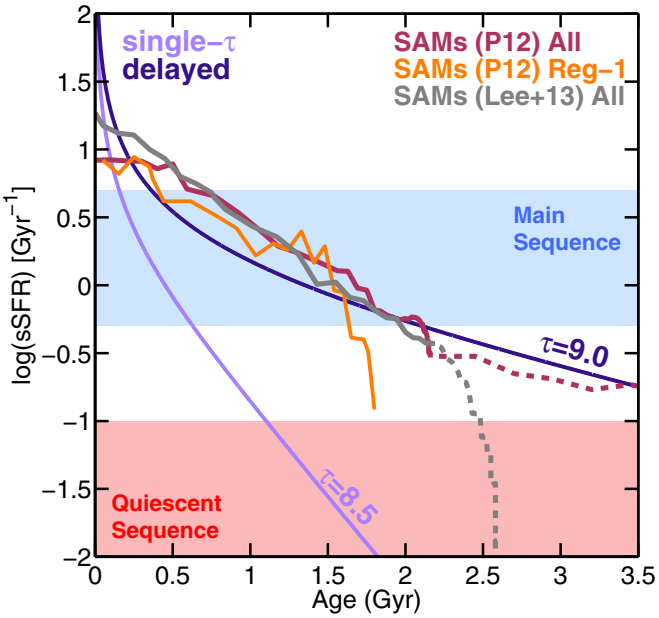

Figure 11. Evolution of the sSFR as a function of time for different SFHs. The light-purple line shows a single τ model with a fast decline, $\tau = 300$ Myr (the typical value for compact SFGs). The dark-purple line shows a delayed model with slow decline, $\tau = 1$ Gyr. The solid magenta/black lines show the averaged, best-fit SAM SFHs for all compact SFGs using the libraries of Pacifici et al. (2012) and Lee & Yi (2013), respectively. Both libraries find similar SFHs, but different forward evolution (dashed lines). The library of Lee & Yi (2013), consisting exclusively of simulated galaxies that are quenched by $z \sim 2$, predicts shorter quenching times. The orange line shows the SAM SFH of the (low-sSFR) compact SFGs in region 1 of the *UVJ* (Figure 3(b)), which present an abrupt decay, compared to the average evolution of compact SFGs.

(A color version of this figure is available in the online journal.)

This suggest that an increasing SFR is more appropriate to reproduce the early phases of stellar mass growth (e.g., Maraston et al. 2010). In that regard, the tracks of the SAM SFHs (right panel of Figure 9) produce slightly better results, following more closely the observed slope of the main sequence at $2 < z < 3$ (see also Pacifici et al. (2013) for a similar result at $z \sim 1$). Figure 10 shows the average slope of those evolutionary tracks for all compact SFGs. While single and delayed τ models present a nearly constant slope at early times of $\alpha = 0$ and $\alpha = 0.5$, respectively, the evolutionary tracks of SAM SFHs present, on average, a steeper slope of $\alpha = 0.65$ and a broader range of values, $\alpha \sim 0.5$–1, closer to the observed slope of the main sequence at lower stellar masses. For both τ models, the slope varies less than 0.05 dex until it starts to roll over at $\log(M/M_{\odot}) \gtrsim 10$. The difference between τ models and SAM SFHs arises from a more gradual increase of the SFR at early times ($t \lesssim 500$ Myr) in SAM SFHs (Figure 8).

Figure 11 shows the evolution of sSFR versus time for the different SFHs. The shaded regions indicate the approximate location of the star-forming main sequence and the quiescent sequence, defined by a range in sSFR. The longer formation timescales of SAM SFHs compared to the τ models lead to a longer duration of the main-sequence phase, $t_{\rm MS} = 1.5$ Gyr (magenta/gray lines). To obtain a similarly long main-sequence phase with delayed models would require e-folding times of 1 Gyr (dark-purple line). However, the majority of compact SFGs are best fitted with much shorter timescales (~300 Myr), which result in an average duration of the main sequence of $t_{\rm MS} < 600$ Myr (light-purple line).

5.1.2. Quenching Times and Migration to the Red Sequence

Not surprisingly, if we extrapolate the SFHs to estimate the quenching times, i.e., the time since the epoch of observation until the galaxy becomes quiescent ($\log(\mathrm{sSFR/Gyr^{-1}}) = -1$), $t_{\rm q} = t_{\rm obs} - t_{\rm quiescent}$, we also obtain significantly larger average values for the P12 SAM SFHs ($t_{\rm q} = 2.5$ Gyr) compared to single ($t_{\rm q} = 300$ Myr) and delayed ($t_{\rm q} = 600$ Myr) τ models. We note, however, that this trend is strongly dependent on the choice of the library of SAM SFHs. The P12 library was created for the analysis of *local* galaxies and therefore favors long-lived SFHs, similar to those of main-sequence galaxies at $z = 0$. If we build a library of SEDs including only galaxies that have low sSFR ($\log(\mathrm{sSFR/Gyr^{-1}}) < -1$) at $z = 2$, the predicted quenching times became substantially shorter ($t_{\rm q} = 400$ Myr; magenta versus gray dashed lines in Figure 11). For this purpose, we used a slightly different SAM (Lee & Yi 2013) because it allowed a simpler selection of the library of quenched galaxies by $z = 2$. As shown by the good agreement between the solid gray and magenta lines in Figure 11, the best-fit SFHs from this library and that of P12 are fully consistent. Only the forward evolution of the SFH differs. Individual examples of short SFHs can be found in the P12 library. For example, the orange line shows the rapid decline in the sSFR of compact SFGs in region 1 ($t \sim 1.8$ Gyr). However, if the galaxy presents a high current SFR, the P12 library usually favors a long-lived forward evolution over a short one.

Although this test shows that the extrapolated SFHs have limited predictive power (i.e., the results depend on the model choice), we can test whether, assuming any of the previous SFHs, it is possible to reproduce the emergence of the quiescent population in terms of quenched compact SFGs. In B13 we showed that the number densities of these two populations are in good agreement for quenching times between $t_{\rm q} = 300$ and

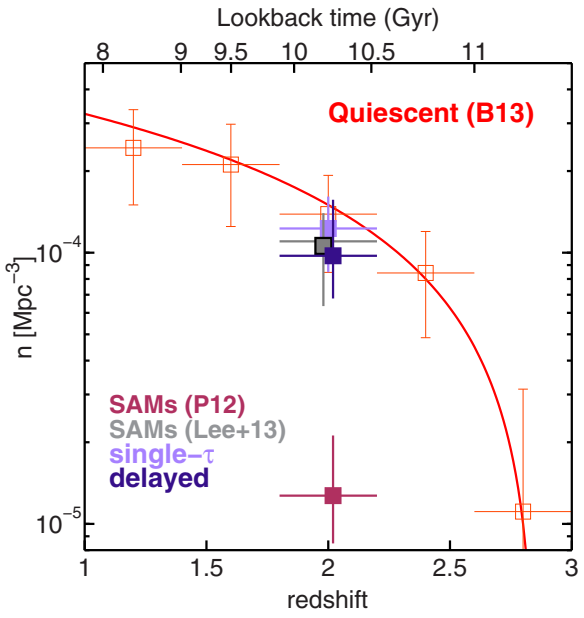

Figure 12. Comparison of the observed number density of compact quiescent galaxies from Barro et al. (2013; red squares and best-fit line) with the predicted number of compact SFGs that would be quenched by that time. We estimate this number extrapolating the best-fit SFHs to single (light-purple) and delayed (dark-purple) τ models, and with SAM SFHs from Pacifici et al. (2012, magenta) and Lee & Yi (2013, black). All the SFHs except those based on the P12 library, which decline more slowly (dashed magenta line in Figure 11), match the observations. This implies that to reproduce the emergence of the quiescent population using SAM SFHs, compact SFGs must experience an abrupt decline of the SFR.

(A color version of this figure is available in the online journal.)

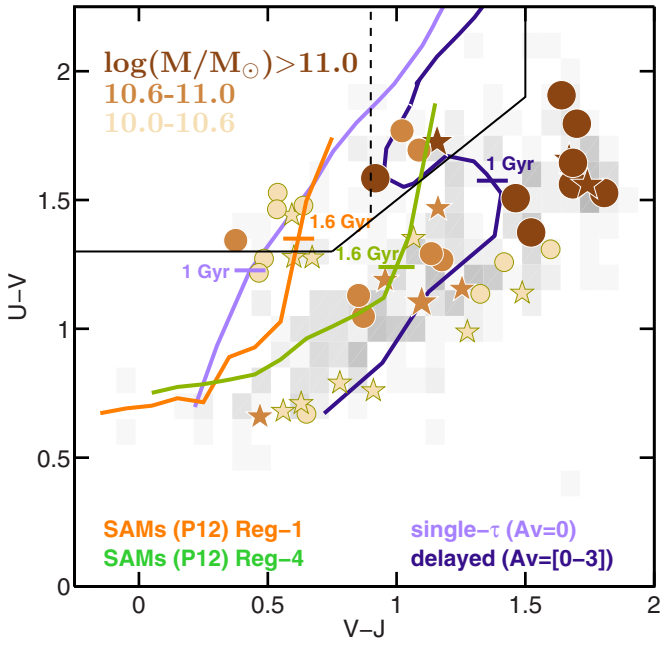

Figure 13. Distribution of the compact SFGs in the *UVJ* diagram for different bins of stellar mass. The boxed gray scale shows other massive ($\log(M/M_\odot) > 10$) SFGs at the same redshift. The low-sSFR, low-extinction galaxies in region 1 (see Figure 3(b)) have lower stellar masses than the majority of compact SFGs. This suggests that there are different tracks to the quiescent region with different dust formation histories. To illustrate this idea, the light-purple line shows the color track of a dust-free single τ model, while the dark-purple line shows a delayed model with variable dust extinction modeled after the SFH (ranging from $A_V = 0$ to 2, and then 0.5 at $\log(\mathrm{sSFR/Gyr^{-1}}) = -1$). Similarly, the orange (green) line shows the SAM SFH color track of a compact SFG in region 1 (region 4) of the *UVJ*. For the SAM SFHs we also model the evolution of the dust extinction after the SFH.

(A color version of this figure is available in the online journal.)

800 Myr (see also Williams et al. 2014). Figure 12 shows that the single and delayed τ models predict number densities that are also consistent with, or slightly lower than, the observed value. For SAM SFHs, however, there is a strong dichotomy depending on which template library we use. While the default (long-lived) templates underpredict the number density by more than an order of magnitude, the short-lived templates are in good agreement with the observations. If, as argued above, SAM SFHs are better at describing the evolutionary paths of compact SFGs, this implies that, to reproduce the emergence of the quiescent population, these galaxies would have to end their lives with a sharp truncation of the SFR on a short timescale compared to their average age ($t_q \sim 400$ Myr over $t = 2$ Gyr; see also Stefanon et al. (2013) for a similar argument). This could indicate the action of a strong quenching mechanism triggered (or enhanced) by the transformation from the extended to the compact phase.

We note that the longer SFHs for compact SFGs, as well as their quiescent descendants, predicted by the SAMs are not inconsistent with the formation timescales inferred from the analysis of chemical abundance patterns in local ellipticals. The latter suggest that the most massive ellipticals had formation timescales between $\Delta t = 300$ and 800 Myr (e.g., Thomas et al. 2005; Johansson et al. 2012; Conroy et al. 2014), which roughly spans the range of plausible e-folding times for τ and delayed SFH in Figure 12. For a truncated SAM SFH (gray line) the assembly is even faster, and the age difference between a τ and an SAM model for a recently quenched ($\log(\mathrm{sSFR/Gyr^{-1}}) = -1$) galaxy is of the order of ~1.5 Gyr. Such small age difference is hard to resolve in old ($t = 10$–12 Gyr) local ellipticals due to intrinsic degeneracies in other modeling parameters such us metallicity, IMF, or the stellar libraries (Conroy et al. 2009).

5.2. Evolutionary Paths in the UVJ Diagram

Figure 13 shows the *UVJ* diagram for compact SFGs color-coded by stellar mass. As discussed in Section 3.2, we find a strong correlation between stellar mass and extinction ($\propto V - J$; see also Wuyts et al. 2011b; Brammer et al. 2011). We also find that nearly all compact SFGs in region 1 belong in the lowest stellar mass bin ($\log(M/M_\odot) = 10$–10.6). As shown in the previous sections, these galaxies appear to have shorter formation timescales and younger ages than other compact SFGs. Recent studies of the stellar populations of quiescent galaxies at $z \sim 2$ report a similar correlation between age and stellar mass (Whitaker et al. 2012a, 2013; Newman et al. 2014a). In those cases, however, the older galaxies are also more quiescent (i.e., with lower sSFRs and redder colors), whereas for compact SFGs, this correlation is reversed. The more massive (older) galaxies are forming stars more actively than the lower-mass ones. This result suggests that at least some low-mass compact SFGs arrive onto the red sequence before the more massive ones, thus populating faster the intermediate- to low-mass end of the quiescent stellar mass function (e.g., Tomczak et al. 2014).

We speculate that the age difference leads to different evolutionary tracks for compact SFGs in the *UVJ* diagram depending on their stellar mass. The more massive, long-lived SFGs undergo active star formation for a longer duration, thus

gradually increasing the amount of dust (produced in supernovae and late phases of stellar evolution) and reaching higher levels of extinction. On the contrary, low-mass compact SFGs have shorter formation timescales and thus exhibit a smaller range of extinctions before shutting down star formation. Regardless of the final stellar mass, however, the amount of dust must decrease prior to quenching to be able to match the low extinction observed in quiescent galaxies.

To illustrate these possibilities, Figure 13 shows the evolutionary tracks for different SFHs with variable levels of dust extinction. For simplicity, we model the evolution of the extinction after the SFHs (i.e., the $A_V \propto$SFR). This parameterization reproduces, qualitatively, the observed correlation between SFR (mass) and obscuration and leads to lower A_V after quenching. Although this model is not exhaustive (see, e.g., Zahid et al. 2013 for detailed modeling based on a similar hypothesis), it provides a simple way to study plausible evolutionary tracks in the *UVJ* diagram. The light-purple line shows the simplest case of a single τ model with no extinction. The dark-purple line shows a delayed model where the dust extinction ranges from $A_V = 0$ to 3 mag. The orange and green lines show the color tracks based on the best-fit SAM SFHs for a compact SFG in region 1 and another one in region 4. In this case, we normalize the extinction to match the best-fit A_V of the galaxies at the time of observation. The difference between these tracks is that the low-mass galaxy (orange) has a shorter star-forming phase and thus reaches lower extinction levels and bluer $V-J$ colors than the more massive galaxy (green). Each evolutionary track indicates the point where the galaxies are 1.6 Gyr old. At that age, the galaxy in region 1 is nearly quiescent and unobscured, while the galaxy in region 4 is still star-forming and has an $A_V = 1.6$ mag. For comparison, the evolutionary tracks for single and delayed τ models with $\tau = 300$ Myr reach the quiescent region earlier at ages of $\sim$1 Gyr.

Overall, the evolutionary tracks reproduce well the observed location in the *UVJ* diagram of the compact SFGs and their quiescent descendants. The only exceptions are the most extinguished galaxies in region 5, whose location on the *UVJ* diagram is, at least partially, the result of inclination effects (see Section 3.2). We note also that a diminishing extinction level following the shutdown of star formation in the most massive galaxies is consistent with the observations of faint IR detections in *UVJ*-quiescent galaxies reported in previous works (Pérez-González et al. 2008b; Brammer et al. 2011). Similarly recent spectroscopic observations indicate that recently quenched galaxies span a broad range of rest-frame $U-V$ colors, suggesting that they can indeed arrive on the red sequence through a more dusty track (Bezanson et al. 2013).

6. THE FORMATION OF COMPACT SFGs

The remarkably small sizes of compact SFGs are among the strongest evidence in favor of their evolutionary connection to the quiescent population at $z \sim 2$. In B13 we speculated that such small sizes could be the result of strongly dissipational processes that reduce the effective radius of SFGs with more extended light profiles. Gas-rich major mergers (Springel & Hernquist 2005; Robertson et al. 2006) or disk instabilities (DIs; Dekel et al. 2009b; Ceverino et al. 2010) triggered by strong processes of gas accretion from the halo (Kereš et al. 2005; Dekel et al. 2009a) are plausible mechanisms. Recent results pointing out the paucity of major mergers at $z = 2$–3 (Williams et al. 2011) and the low incidence of merging signatures on compact SFGs and quenched galaxies (Kaviraj et al. 2013b) seem to favor internal, self-regulated mechanisms like DIs. However, direct evidence of the mechanisms responsible for the formation of compact SFGs remains to be found.

Cosmological simulations of galaxy formation provide a perfect framework to test different scenarios and make predictions about which galaxies are likely to experience significant structural transformations. In this section we present the results of two sets of theoretical models, namely, the recent SAMs of Porter et al. (2014a) and a set of hydrodynamical simulations described in Ceverino et al. (2010). Note that the SAMs discussed in this section are different from those used in Section 4.3. The latter were preferred for the analysis of the stellar populations, as they were described and exhaustively tested for that purpose in Pacifici et al. (2012, 2013). However, the SAMs of Porter et al. (2014a) include new physical prescriptions critical for the formation of compact SFGs and thus are more suitable for the study of structural evolution. We are now working to incorporate the new SAMs into the code used for stellar population analysis.

6.1. Compact SFGs in the SAMs of Porter et al. (2014a)

A full description of the semianalytic recipes and the accuracy of the models to reproduce observational trends at low and high redshifts is presented in Porter et al. (2014a, 2014b) and L. A. Porter et al. (2014, in preparation). Briefly, these SAMs are an extension of those presented in Somerville et al. (2008, 2012), which included prescriptions for radiative cooling, star formation, supernova and black hole feedback, as well as chemical enrichment and galaxy mergers. A novel feature of the new version is the addition of dissipational processes, critical for the formation of spheroidal galaxies. In particular, these SAMs include a new treatment of gravitational perturbations that allows the formation of star-forming clumps and the triggering of DIs. These result in the inward migration of gas and clumps to the center, making the galaxy more compact (Ceverino et al. 2012; Dekel et al. 2013). DIs are modeled using the Toomre (1964) instability criterion. If a galaxy exceeds the critical threshold, a fraction of the total stellar mass is removed from the disk and added to the central (bulge) component, thereby reducing the half-light (and half-mass) radius. Although a detailed characterization of the DI requires high-resolution simulations (see next section), the Toomre criterion allows one to quickly test a plausible formation scenario for compact SFGs that is consistent with the observational picture of unstable clumpy disks (Elmegreen & Elmegreen 2005; Genzel et al. 2008; Förster Schreiber et al. 2009).

The left panel of Figure 14 shows the predicted evolutionary tracks in the mass–size diagram for three simulated galaxies that satisfy the compact SFG selection criteria at $z = 2$–3 (blue lines). For comparison, we also show the tracks for a group of noncompact SFGs at the same redshift (green lines). All compact SFGs experience a significant shrinkage in effective radius of a factor of $\sim$2, increasing the mass surface density beyond the compactness threshold (dashed line). According to L. A. Porter et al. (2014, in preparation), all galaxies in the compact region are the result of a dissipational process, either DIs (60%) or major mergers (40%). Overall, the remnants of DIs are 10% more compact than those of mergers and thus are more efficient at populating the region of highest Σ. In the SAMs, the contraction enhances the strength of the quenching mechanisms responsible for shutting down star formation. In particular, most compact SFGs quench on timescales of a few hundred Myr as a result of quasar mode feedback. These numbers are consistent with the quenching timescales estimated in Section 5.1.

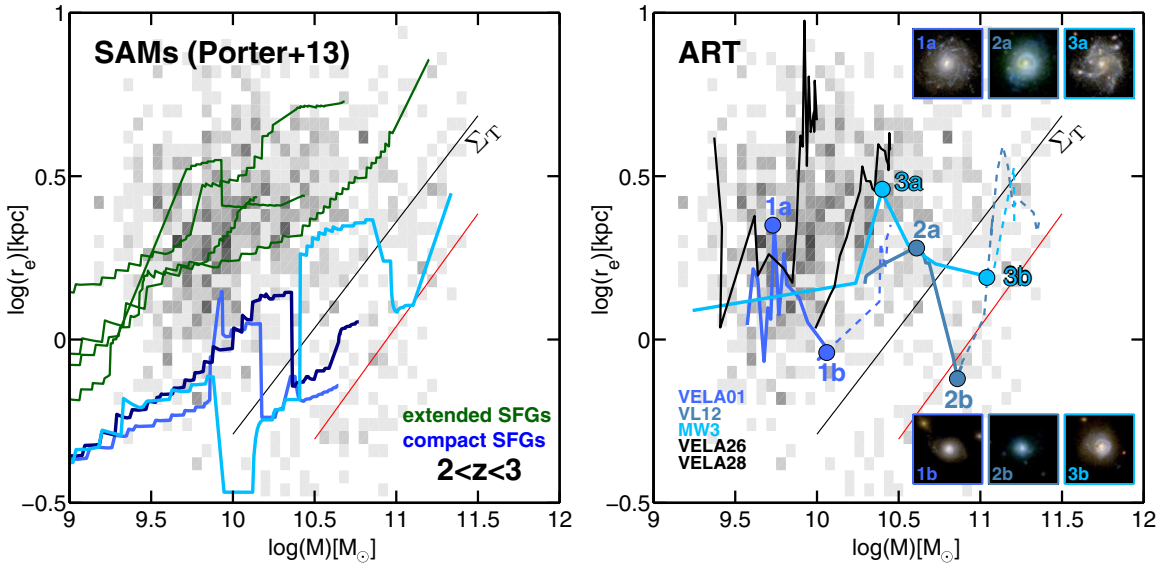

Figure 14. Comparison of the observed galaxy distribution in the mass–size diagram at $2 < z < 3$ (boxed gray scale) with the predictions from theoretical models (colored tracks). The black line indicates the selection criteria, $\log(\Sigma_T / M_\odot\ \mathrm{kpc}^{1.5} = 10.3)$, for compact galaxies (below the line), and the red line the average mass–size relation for quiescent galaxies at $z \sim 2$ (Newman et al. 2012). Left panel: the green lines show the evolutionary tracks (since the onset of star formation until $\log(\mathrm{sSFR/Gyr}^{-1}) < -1$) of three noncompact SFGs in the SAMs of Porter et al. (2014a). The evolution of these galaxies is consistent with the mass–size correlation for the bulk of SFGs. The blue tracks show the evolution of three galaxies selected to satisfy the compact SFG criterion at $2 < z < 3$. All these galaxies become compact as a result of DIs that cause a sharp contraction in the r_e by a factor of ∼2. Right panel: the blue lines show the evolutionary tracks of three galaxies drawn from the sample of hydrodynamic simulations of Ceverino et al. (2012). All these galaxies experience a significant shrinkage due to DIs. For comparison, the black lines show two other galaxies from that sample that have fluctuations in size but maintain an overall size-growing trend. The $5'' \times 5''$ kpc stamps illustrate the visual appearance of these galaxies at the stages of maximum r_e (disk-like and clumpy; 1a, 2a, 3a) and minimum r_e (compact spheroid; 1b, 2b, 3b).

(A color version of this figure is available in the online journal.)

An interesting prediction of the models is that the precursors of compact SFGs are usually among the smallest galaxies for a given stellar mass, even before the dissipational process, i.e., they are on the lower envelope of the mass–size relation for SFGs (Figure 14). They also present the highest sSFRs at a given mass, which, combined with their small sizes, makes them more susceptible to the Toomre instability.

6.2. Compact SFGs in Hydrodynamic Simulations

Hydrodynamic simulations provide a high-resolution view of the processes shaping galaxy structure (gas inflow, DIs, galaxy interactions, etc.), which is unavailable in the SAMs. Unfortunately, such detailed simulations require large computational efforts, which are only possible for small samples of ∼30–50 galaxies. Here we focus on a handful of galaxies drawn from the larger sample of Ceverino et al. (2010, 2014) and Dekel et al. (2013), computed with the Adaptive Refinement Tree code (Kravtsov et al. 1997) using spatial resolutions ranging between 17 and 75 pc (see Ceverino & Klypin 2009 for more details about the code). To ensure a fair comparison between models and observations, the structural properties of the simulated galaxies are measured using GALFIT on images processed to emulate the properties of the CANDELS data. This includes degrading the high-resolution simulations down to $0\farcs06$ pixel^{-1}, convolving with the PSF of the F160W image, and adding random noise to emulate the S/N of the real data (M. Mozena et al. 2014, in preparation).

The right panel of Figure 14 shows the evolutionary tracks of the simulated galaxies in the mass–size diagram. The blue lines depict the only three galaxies in the sample that present (at some point) a decrease in effective radii larger than a factor of two, over a period of time of at least 300 Myr (i.e., we reject rapid fluctuations that last only for one or two simulation time steps). The shrinkage is large enough to be significant, and it is similar to the decrease in r_e experienced by compact SFGs in the SAMs. For comparison, the black lines illustrate the evolution of other simulated galaxies showing milder size fluctuations. Interestingly, none of the three compact galaxies experienced a major merger. In all cases, the shrinkage appears to be the result of DIs. As a result, the star-forming clumps (clearly seen in the high-resolution images of Figure 14; Moody et al. 2014), along with large amounts of gas, migrate inward due to dynamical friction and tidal torques generated by the unstable disk (e.g., Dekel et al. 2009b; Bournaud et al. 2011). In the center, the gas is turned into stars very efficiently, causing a significant increase in the inner stellar mass (∼0.3–0.5 dex) at the same time that the size of the galaxy decreases. In the compact stage, the galaxies are more centrally concentrated and show no evidence of star-forming clumps. In terms of their light profiles, during and after the contraction, we find that the Sérsic index increases from low (n = 1–2) to high ($n > 3$) spheroid-like values (see also Ceverino et al. 2014; A. Zolotov et al. 2013, in preparation). The whole transformation process from extended, clumpy disk to compact spheroid occurs on timescales of a few hundred Myr, i.e., of the order of the dynamical timescale of the disks (Ceverino et al. 2010; Cacciato et al. 2012). This is consistent with the scenario proposed in B13 in which new compact SFGs are being formed at a similar pace at which the existing ones are turning quiescent.

Based on analytic calculations, Dekel & Burkert (2014) showed that the process of disk contraction due to DIs is expected to happen for nearly half of the massive SFGs at $z \gtrsim 2$. Such a high fraction results from a combination of high SFRs and continuous gas accretion common at these redshifts. The ratio of the timescales of these processes, $w = t_{\mathrm{SF}}/t_{\mathrm{infall}}$ (*wetness* parameter), controls the DI process. For $w > 1$ the

galaxy triggers a dissipative wet inflow, becoming more compact and centrally concentrated, whereas for lower values it forms the new stars in an inside-out growing disk. The duration of the DI phase determines whether the galaxy shrinks enough to become a compact SFG or it grows in size again after the contraction (i.e., the $w < 1$ mode). The answer to this question depends on the process that regulates star formation (internal quenching) and gas infall (halo quenching). For example, the version of the simulations used in this paper does not include the effects of radiation feedback, from either AGN or star formation, and thus galaxies are unlikely to experience a severe suppression of SFR (Dekel et al. 2013) after the shrinkage. In fact, all of them tend to regrow an extended disk component. This is illustrated by the dashed lines in Figure 14, which show a rapid increase in effective radii of the compact SFGs shortly after the contraction. The relevance of these hydrodynamical simulations for compact SFG formation is thus the physics and duration of the event, not the total evolutionary picture.

7. SUMMARY

1. We analyze the SFRs, structural properties, and stellar populations of 45 massive ($\log(M/M_{\odot}) > 10$) compact SFGs at $2 < z < 3$ in GOODS-S to extend the results of Barro et al. (2013) and present further evidence that these galaxies are the natural progenitors of the compact, quiescent galaxies at $z \sim 2$.
   (a) Compact SFGs present heavily obscured star formation based on their *Spitzer*/*Herschel* far-IR colors (71% and 44%/13% are detected in MIPS and PACS/SPIRE). As a group, they exhibit a higher fraction of X-ray-detected AGNs (47%) than more extended SFGs (12%) or quiescent galaxies (9%) at the same redshift and stellar mass. Such a high fraction implies that compact SFGs are typically in an active phase of black hole growth.
   (b) The distribution of compact SFGs in the SFR–M diagram extends from the *normal* main sequence (65%) to nearly the region occupied by quenched galaxies (30%). This result is consistent with the notion that these galaxies are in transit to become compact, quiescent galaxies. Only 2/45 compact SFGs lie above the SFR–M main sequence, and they present far-IR SEDs typical of a *starburst* galaxy. Such a small fraction suggests that either the transition from star-forming to quiescent does not require an abrupt burst of star formation, or the *starburst* duty cycle is very short, ∼5% the duration of the main-sequence phase.
   (c) The transiting nature of compact SFGs is further supported by their location in the *UVJ* diagram, where most compact SFGs lie within the dusty, reddened region occupied by other massive SFGs, while those with lower sSFRs scatter off toward the quiescent region.
   (d) The radii, Sérsic indices, axial ratios, and spheroidal morphologies of compact SFGs match well to those of the quiescent galaxies and indicate that they can directly evolve into the red population simply by shutting down their star formation.
   (e) The structural properties of compact SFGs are strikingly different from those of noncompact SFGs, which have disk-like morphologies and usually clumpy or irregular appearance. Under the assumption that galaxies grow in both stellar mass and size during the star-forming phase, the progenitors of massive ($\log(M/M_{\odot}) > 10$), compact SFGs are probably among these extended SFGs. This suggests the need for a transformation mechanism to link the two populations that shrinks the size and transforms the structure of extended galaxies from disk to spheroid (see point 3).
2. We study the stellar populations of compact SFGs using two sets of SFHs: (1) exponentially declining (single and delayed) τ models and (2) a library of physically motivated SFHs extracted from SAMs. Qualitatively, both sets of SFHs produce similar results and trends; however, they differ in their quantitative predictions.
   (a) SAM SFHs predict longer formation timescales and older ages, $t = 2^{+0.4}_{-0.2}$ Gyr ($z_{\rm form} = 6$–7), which are nearly a factor of two older than the estimates of single, $t = 0.9^{+0.2}_{-0.5}$ Gyr, and delayed, $t = 1.1^{+0.2}_{-0.6}$ Gyr, τ models ($z_{\rm form} = 3$–4). Both τ models and SAM SFHs provide similarly good SED fits in terms of reduced χ^2 and statistical errors. Therefore, the difference in the best-fit age reflects also the order of magnitude of the systematic uncertainties caused by the degeneracies associated with the lack of knowledge of the true SFHs.
   (b) We place additional constraints on the most likely SFHs for compact SFGs from the analysis of their evolutionary tracks in the SFR–M diagram. We find that tracks of the SAM SFHs provide a better description of how compact SFGs evolve as a function of time, by tracking more closely the observed slope of the main sequence, X versus Y, Z in the τ models, and by remaining on it for ∼70% of their lifetime, versus $\lesssim$20% in the τ models.
   (c) We find that some low-mass, compact SFGs ($\log(M/M_{\odot}) = 10$–10.6) have younger ages and undergo active star formation for a shorter duration than more massive SFGs, suggesting that they arrive earlier onto the red sequence. Thus, we speculate that compact SFGs follow different evolutionary tracks on the *UVJ* diagram depending on their stellar mass. These tracks differ in the amount of dust extinction, whose amount varies according to the SFR: more massive galaxies increase their dust content gradually during a longer star-forming phase, thus reaching higher levels of extinction, whereas lower-mass galaxies have shorter formation timescales and thus evolve (faster) on a lower extinction track.
   (d) Both sets of SFHs are able to reproduce the number density of compact quiescent galaxies at $z = 2$ from compact SFGs quenching on timescales of $t_{\rm q} =$ 300–600 Myr. In τ models, these quenching times are the result of a rapid assembly, $\tau \sim 300$ Myr, whereas SAM SFHs predict a gradual assembly followed by an abrupt decay, 4× shorter than the duration of the star-forming main-sequence phase ($t_{\rm MS} = 1.5$ Gyr).
3. To analyze the proposed evolutionary sequence from extended to compact SFGs, we study the formation mechanisms of compact SFGs in theoretical models of galaxy formation.
   (a) The recent SAMs of Porter et al. (2014a) suggest that compact SFGs form only in strongly dissipational processes, such as major mergers or DIs. However,

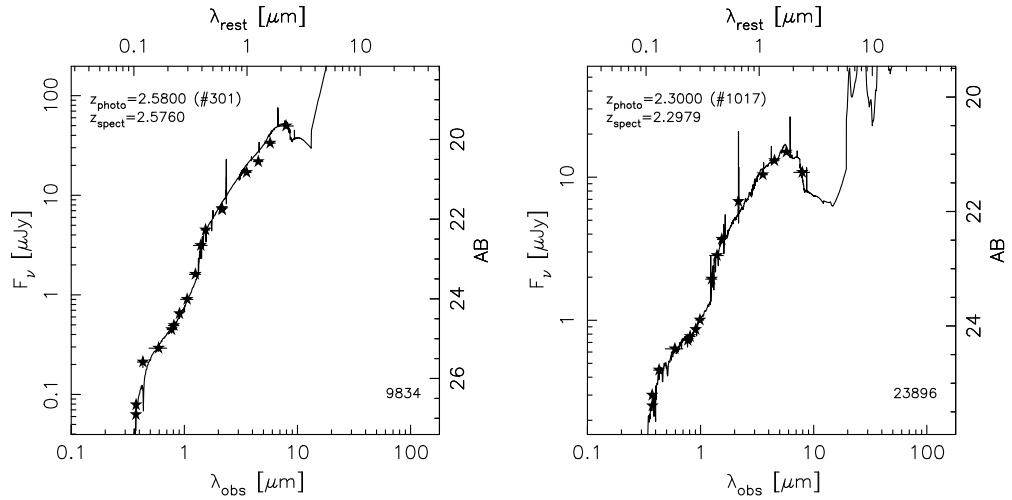

Figure 15. SEDs of compact SFGs hosting an AGN, and their best-fit optical–NIR templates. Left panel: fitting the SED requires a hybrid model combining a stellar component (60%) plus an AGN component (40%). The AGN contribution is more prominent in the rest-frame NIR (the 1.6 μm bump is slightly shifted redward), but the hybrid template suggests that there is also some contribution of the AGN to the rest-frame UV luminosity (L. Hsu et al. 2014, in preparation, will present the analysis of the SEDs of the AGNs in GOODS-S using hybrid templates). Right panel: the SED is well fitted with a pure stellar component template.

DIs are more frequent (60% versus 40%) and form the majority of the most compact remnants.

(b) Compact SFGs formed in DIs are among the smallest SFGs of a given stellar mass before the contraction, and, after the DI, they experience a contraction in r_e by a factor of two.

(c) We verify these SAM predictions by using the high-resolution hydrodynamic simulations of Ceverino et al. (2012), where we find three representative examples of compact SFGs formed in DIs. These galaxies experience a similar size shrinkage while changing their morphology from clumpy disk to centrally concentrated spheroid. This contraction is also in good agreement with recent predictions from Dekel & Burkert (2014) and A. Zolotov (in preparation) for the effect of DIs.

We thank David Elbaz for very useful discussions. Support for Program number HST-GO-12060 was provided by NASA through a grant from the Space Telescope Science Institute, which is operated by the Association of Universities for Research in Astronomy, Incorporated, under NASA contract NAS5-26555. G.B. acknowledges support from NSF grant AST-08-08133. P.G.P.-G. acknowledges support from grant AYA2012-31277-E. This work has made use of the Rainbow Cosmological Surveys Database, which is operated by the Universidad Complutense de Madrid (UCM), partnered with the University of California Observatories at Santa Cruz (UCO/Lick, UCSC). C.P. acknowledges the support by the KASI-Yonsei Joint Research Program for the Frontiers of Astronomy and Space Science funded by the Korea Astronomy and Space Science Institute. J.L. acknowledges the support by the National Research Foundation of Korea through the SRC grant to the Center for Galaxy Evolution Research and the Doyak grant (No. 20090078756).

APPENDIX A

TESTING AGN CONTAMINATION IN THE SEDs

We fit the SEDs of the 21/45 X-ray-detected compact SFGs galaxies with the AGN templates of Salvato et al. (2009, 2011) to identify a possible AGN contamination in the stellar SED. We find that four galaxies, best fitted with Type I AGN templates, present strong continuum contamination from the nonstellar component and IRAC power-law slopes. Another three are fitted with composite Type 2/stellar templates, suggesting that a minor AGN contamination could be possible. To test this effect, we compare the stellar masses of the 21 galaxies derived from stellar templates with those of Santini et al. (2012) calculated using a combination of stellar and nuclear (Silva et al. 2004) components. In agreement with the previous analysis, we find a significant offset in the stellar masses ($\Delta M_\star = 0.3$ dex) of the four aforementioned Type I AGNs, while for the other three galaxies the contamination is small, and the stellar masses differ by less than 0.1 dex. The left panel of Figure 15 illustrates the SED of a compact SFG with a significant (∼40%) AGN contribution to the SED. The right panel shows the SED of another X-ray-detected compact SFG whose SED is well fitted by a pure stellar component. Based on the results of the SED fitting to hybrid stellar+AGN templates, we exclude the four strongly contaminated galaxies (indicated in Table 1) from the analysis in Sections 3 and 4.

APPENDIX B

SFR_{IR+UV} VERSUS SFR MODEL CONSISTENCY

In the following we assess the agreement between SFR_{IR+UV} and SFR model for different SFHs. While SFR_{IR+UV} is, arguably, the best SFR indicator for heavily obscured galaxies, SFR model is tied to all other stellar properties (age, quenching time, etc.), and thus a fully consistent analysis of the galaxy properties requires a good match between both SFR indicators.

B.1. Constrained τ Models

As shown in Wuyts et al. (2011a), the motivation for constraining the *e*-folding time to be larger than $\tau = 300$ Myr (i.e., rejecting quasi-instantaneous bursts) is to obtain a better agreement between SFR_{IR+UV} and SFR model. Otherwise, the SED fits tend to favor solutions with shorter formation timescales, which lead to SFR model systematically lower than SFR_{IR+UV}.

The left panel of Figure 16 shows the comparison of SFR_{IR+UV} and SFR model for compact SFGs based on constrained single τ models. Overall, the agreement is quite good, and the scatter is

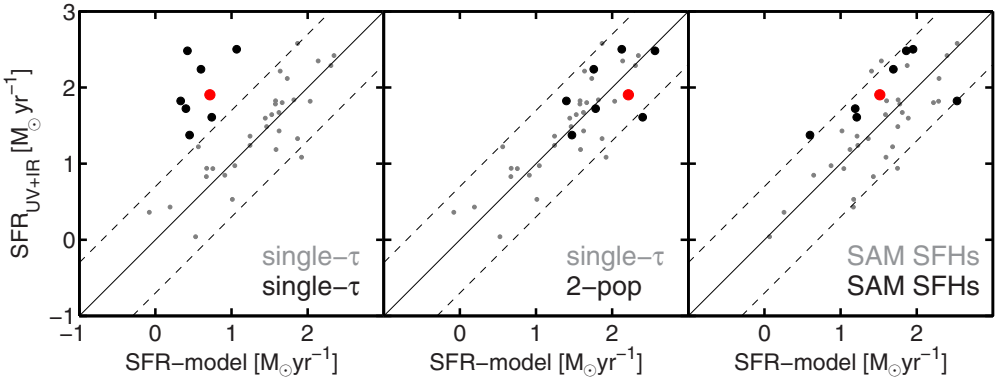

Figure 16. Comparison between SFR_{IR+UV} and the SFR model for compact SFGs. Each panel illustrates the comparison for SFR model derived from different SFHs. Left panel: single τ models; the overall agreement between SFR estimates is good, but there are some outliers (black) for which SFR model $\ll SFR_{IR+UV}$. These appear to be either extremely obscured galaxies with high SFRs or galaxies with lower SFRs for which the last (obscured) burst of star formation is shutting down. In both cases the best-fit τ model is too old (low sSFR) to match the observed SFR_{IR+UV}. Central panel: two-population τ models; Using a composite stellar population consisting of a relatively old underlying population plus a young, obscured burst provides a better agreement between the two independent SFR indicators. Right panel: SAM SFHs; using these models, the agreement in the SFRs is better than for single τ models and similar to the two-population case. For most of these galaxies the SAM SFHs feature a burst of star formation prior to the epoch of observation, similarly to the two-population τ SFHs. The red marker highlights one of the outliers in region 2 of the *UVJ*; Figure 18 shows the best-fit templates for this galaxy based on different SFHs.

(A color version of this figure is available in the online journal.)

consistent with the typical uncertainties in SFRs (rms[SFR] $\sim$ 0.39 dex; e.g., Daddi et al. 2007b). There are, however, a group of galaxies ($\sim$20%) that present significantly lower values of SFR model compared to SFR_{IR+UV} (ΔSFR $>$ 1 dex). These discrepancies have been reported in previous works, where the authors attributed them to cases of high dust obscuration in which reddening saturates as an extinction indicator (Santini et al. 2009; Reddy et al. 2010). In such cases, the Calzetti et al. (2000) attenuation law fails to provide a realistic approximation, and the additional reddening is compensated by the models aging the stellar populations, i.e., they are fitted with old stellar populations instead of young and dusty ones. We find the same systematic outliers if we use delayed models instead of single τ. These outliers are preferentially located in regions 2 (dusty + intermediate age) and 5 (highly obscured) of the *UVJ* diagram (Figure 1(b)).

The case of galaxies in region 5 ($V - J$ >1.5) has been discussed in detail in Patel et al. (2012), where the authors show that, in many cases, the high dust obscuration is largely driven by inclination effects. In agreement with this result, we find that compact SFGs in region 5 have small Sérsic indices and lower axis ratios, characteristic of edge-on disks (see Section 3). The outliers in region 2 are mainly IR-detected galaxies located near the quiescent region of the *UVJ* diagram. Similar cases have been reported in other works (e.g., Brammer et al. 2011; Patel et al. 2013), which suggest that the IR luminosity could be powered by either an obscured AGN or the final stages of star formation in quenching galaxy. Only one out of the four galaxies in region 2 of the *UVJ* is an X-ray-detected AGN, but neither that galaxy nor any of the other three present present IRAC power-law SEDs or *Spitzer*/*Herschel* colors indicative of obscured AGN activity. The outliers are always among the largest (r_e > 1.5 kpc), most massive compact SFGs, and their rest-frame UV emission appears to be confined in a small central region. This could be signaling the fading of a nuclear burst, or perhaps that optical and IR emission is associated with physically distinct regions of the galaxy (e.g., an obscured surrounding component).

In order to reconcile the SFR_{IR+UV} and SFR model for the outliers, we first tried to use a different extinction law, namely, Charlot & Fall (2000), which allows for a steeper (less gray) wavelength dependence than Calzetti and thus increases the attenuation in the rest-frame UV. However, the best-fit ages obtained with this approach were only marginally younger, and thus the values of SFR model were still severely underpredicted. As an alternative approach to account for missing star formation, we modeled the SED of the outliers using two single τ models, which represent an intermediate-age, moderate extinction, underlying population, plus a young recent burst with younger age and higher obscuration (see, e.g., Bell 2003; Pérez-González et al. 2008a). In addition, we introduced the far-IR fluxes as a prior, by requiring that the absorbed UV luminosity of the young burst matched the IR emission from the heated dust within a factor of $\sim$2 (see, e.g., da Cunha et al. 2008, 2010 for a similar approach). As shown in the central panel of Figure 16, the two-population approach provides a better agreement between SFR_{IR+UV} and SFR model for the outliers, and therefore we adopted the best-fit stellar properties and SFRs estimated with this method for the analysis in Section 5. Nevertheless, the most significant difference affected the SFR model (ΔSFR of up to 1.5 dex), whereas the masses and stellar ages (of the older component) changed by $\Delta M \sim 0.15$ dex and $\Delta t \sim 0.2$ dex, respectively.

The success of the two-population approach to reconcile the apparent inconsistency between optical and far-IR SEDs could indicate that, at least for some galaxies, the SFHs are not as smooth as single τ models. In fact, in the hierarchical picture of galaxy formation, the SFHs are likely to be more stochastic due to discrete accretion events. The addition of a second population to the SFH provides a first-order approximation to reflect at least the most recent of such events.

B.2. SAMs

Interestingly, using SAM SFHs, which present such stochastic events of star formation, the agreement between SFR_{IR+UV} and SFR model is better than for single τ models. Although the overall scatter is slightly higher than in the single τ models (rms[SFR] $\sim$ 0.43 dex), there are fewer systematic outliers (right

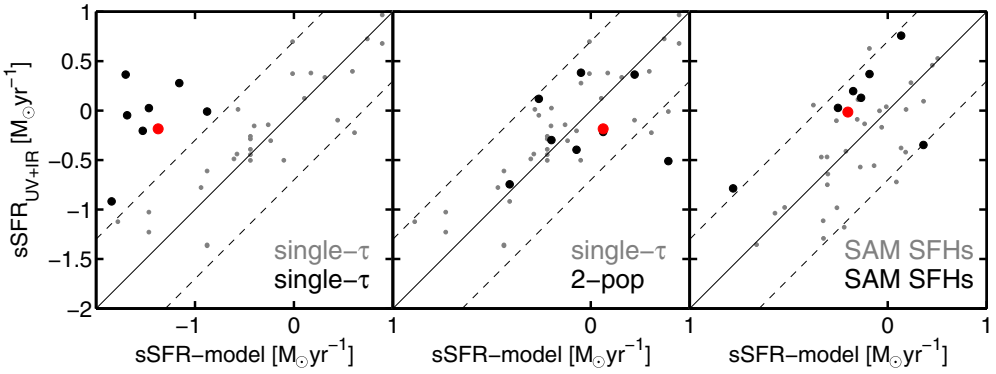

Figure 17. Same as Figure 16, but comparing the sSFR$_{IR+UV}$ and the sSFR model for compact SFGs.
(A color version of this figure is available in the online journal.)

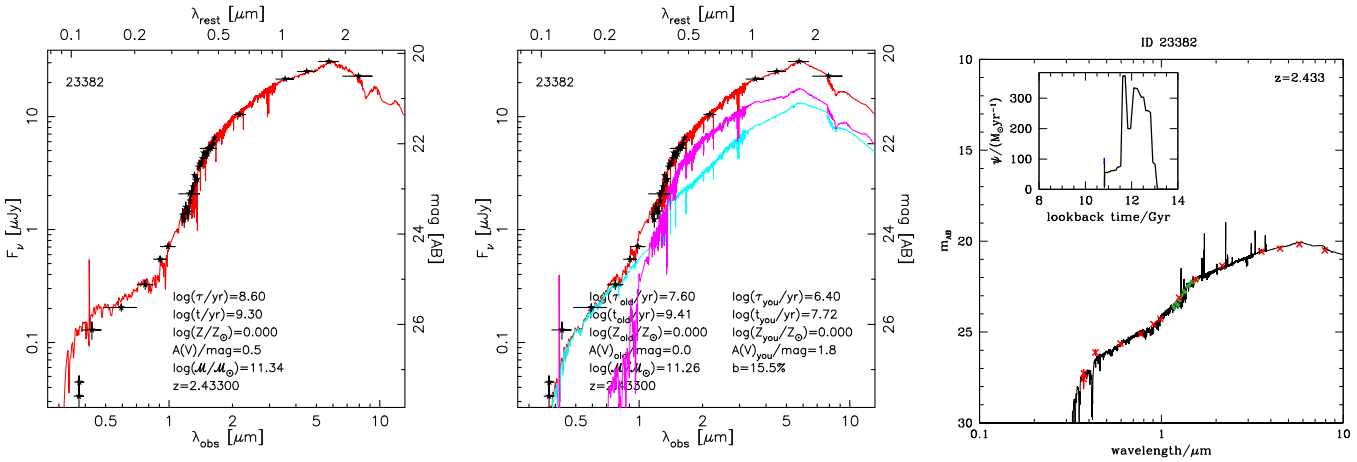

Figure 18. Best-fit stellar templates and inferred stellar properties for one of the outliers in the SFR$_{IR+UV}$ vs. SFR model comparison (ΔSFR > 0.7 dex), marked in red in Figure 16. Left panel: best-fit BC03 model based on a single τ SFH suggests that the galaxy is nearly quiescent (log(sSFR/Gyr^{-1}) = −1) and moderately obscured, which is inconsistent with the high SFR values derived from the IR luminosity, based on MIPS and *Herschel* detections. Central panel: using two single τ models provides a better match between SFR model and SFR$_{IR+UV}$ from a composite stellar population of an old, low-attenuation component (magenta) and a young, obscured component (cyan) with high SFR that would be responsible for the observed IR emission. Right panel: best-fit stellar template based on the SAM SFHs of Pacifici et al. (2012). According to this SFH, the galaxy was at the peak of his SFR 1 Gyr before the epoch of observation. Now the SFR is declining slowly, which provides a good match to SFR$_{IR+UV}$ without any other additional requirements.
(A color version of this figure is available in the online journal.)

panel of Figure 16). Attending to the SFHs of the outliers, we find that, in most cases (∼60%), the good agreement between SFR$_{IR+UV}$ and SFR model is the result of a short burst of star formation in the last 10 Myr (right panel of Figure 18), similarly to what we obtained using the two-population approach. For the rest of the outliers, the values of SFR model are higher because their overall SFHs present a longer duration of the actively star-forming phase and a slower decline of the SFR (i.e., a shallower slope) than the τ models (see, e.g., Figure 7 or Figure 8). Consequently, the SFR remains high for a longer period of time.

REFERENCES

Ashby, M. L. N., Willner, S. P., Fazio, G. G., et al. 2013, ApJ, 769, 80
Baldry, I. K., Glazebrook, K., Brinkmann, J., et al. 2004, ApJ, 600, 681
Balestra, I., Mainieri, V., Popesso, P., et al. 2010, A&A, 512, A12
Barro, G., Faber, S. M., Pérez-González, P. G., et al. 2013, ApJ, 765, 104
Barro, G., Pérez-González, P. G., Gallego, J., et al. 2011, ApJS, 193, 30
Barro, G., Trump, J. R., Koo, P. C., et al. 2014, arXiv:1405.7042
Bauer, A. E., Conselice, C. J., Pérez-González, P. G., et al. 2011, MNRAS, 417, 289
Bedregal, A. G., Scarlata, C., Henry, A. L., et al. 2013, arXiv:1309.3567
Bell, E. F. 2003, ApJ, 586, 794
Bell, E. F., Papovich, C., Wolf, C., et al. 2005, ApJ, 625, 23
Bell, E. F., van der Wel, A., Papovich, C., et al. 2012, ApJ, 753, 167
Bezanson, R., van Dokkum, P., van de Sande, J., Franx, M., & Kriek, M. 2013, ApJL, 764, L8
Bezanson, R., van Dokkum, P. G., Tal, T., et al. 2009, ApJ, 697, 1290
Birnboim, Y., & Dekel, A. 2003, MNRAS, 345, 349
Blain, A. W., Smail, I., Ivison, R. J., Kneib, J.-P., & Frayer, D. T. 2002, PhR, 369, 111
Bournaud, F., Dekel, A., Teyssier, R., et al. 2011, ApJL, 741, L33
Bournaud, F., Jog, C. J., & Combes, F. 2007, A&A, 476, 1179
Bouwens, R. J., Illingworth, G. D., Oesch, P. A., et al. 2012, ApJ, 754, 83
Brammer, G. B., van Dokkum, P. G., & Coppi, P. 2008, ApJ, 686, 1503
Brammer, G. B., van Dokkum, P. G., Franx, M., et al. 2012, ApJS, 200, 13
Brammer, G. B., Whitaker, K. E., van Dokkum, P. G., et al. 2011, ApJ, 739, 24
Bruce, V. A., Dunlop, J. S., Cirasuolo, M., et al. 2012, MNRAS, 427, 1666
Bruzual, G., & Charlot, S. 2003, MNRAS, 344, 1000
Buitrago, F., Trujillo, I., Conselice, C. J., et al. 2008, ApJL, 687, L61
Cacciato, M., Dekel, A., & Genel, S. 2012, MNRAS, 421, 818
Calzetti, D., Armus, L., Bohlin, R. C., et al. 2000, ApJ, 533, 682
Caputi, K. I. 2013, ApJ, 768, 103
Carollo, C. M., Bschorr, T. J., Renzini, A., et al. 2013, ApJ, 773, 112
Cassata, P., Giavalisco, M., Guo, Y., et al. 2011, ApJ, 743, 96
Cassata, P., Giavalisco, M., Williams, C. C., et al. 2013, ApJ, 775, 106
Ceverino, D., Dekel, A., & Bournaud, F. 2010, MNRAS, 404, 2151
Ceverino, D., Dekel, A., Mandelker, N., et al. 2012, MNRAS, 420, 3490
Ceverino, D., & Klypin, A. 2009, ApJ, 695, 292
Ceverino, D., Klypin, A., Klimek, E., et al. 2014, MNRAS, 442, 1545
Chabrier, G. 2003, PASP, 115, 763
Chang, Y.-Y., van der Wel, A., Rix, H.-W., et al. 2013, ApJ, 773, 149

Charlot, S., & Fall, S. M. 2000, ApJ, 539, 718
Chary, R., & Elbaz, D. 2001, ApJ, 556, 562
Cheung, E., Faber, S. M., Koo, D. C., et al. 2012, ApJ, 760, 131
Cisternas, M., Jahnke, K., Inskip, K. J., et al. 2011, ApJ, 726, 57
Conroy, C., Graves, G. J., & van Dokkum, P. G. 2014, ApJ, 780, 33
Conroy, C., Gunn, J. E., & White, M. 2009, ApJ, 699, 486
Cox, T. J., Jonsson, P., Somerville, R. S., Primack, J. R., & Dekel, A. 2008, MNRAS, 384, 386
Croton, D. J., Springel, V., White, S. D. M., et al. 2006, MNRAS, 365, 11
Curtis-Lake, E., McLure, R. J., Pearce, H. J., et al. 2012, MNRAS, 422, 1425
da Cunha, E., Charlot, S., & Elbaz, D. 2008, MNRAS, 388, 1595
da Cunha, E., Charmandaris, V., Díaz-Santos, T., et al. 2010, A&A, 523, A78
Daddi, E., Alexander, D. M., Dickinson, M., et al. 2007a, ApJ, 670, 173
Daddi, E., Dickinson, M., Morrison, G., et al. 2007b, ApJ, 670, 156
Daddi, E., Elbaz, D., Walter, F., et al. 2010, ApJL, 714, L118
Daddi, E., Renzini, A., Pirzkal, N., et al. 2005, ApJ, 626, 680
Dahlen, T., Mobasher, B., Faber, S. M., et al. 2013, ApJ, 775, 93
Davies, R. I., Müller Sánchez, F., Genzel, R., et al. 2007, ApJ, 671, 1388
De Lucia, G., & Blaizot, J. 2007, MNRAS, 375, 2
De Lucia, G., Kauffmann, G., & White, S. D. M. 2004, MNRAS, 349, 1101
Dekel, A., & Birnboim, Y. 2006, MNRAS, 368, 2
Dekel, A., Birnboim, Y., Engel, G., et al. 2009a, Natur, 457, 451
Dekel, A., & Burkert, A. 2014, MNRAS, 438, 1870
Dekel, A., Sari, R., & Ceverino, D. 2009b, ApJ, 703, 785
Dekel, A., Zolotov, A., Tweed, D., et al. 2013, MNRAS, 435, 999
Diamond-Stanic, A. M., Moustakas, J., Tremonti, C. A., et al. 2012, ApJL, 755, L26
Djorgovski, S., & Davis, M. 1987, ApJ, 313, 59
Donley, J. L., Rieke, G. H., Pérez-González, P. G., & Barro, G. 2008, ApJ, 687, 111
Donley, J. L., Rieke, G. H., Pérez-González, P. G., Rigby, J. R., & Alonso-Herrero, A. 2007, ApJ, 660, 167
Elbaz, D., Daddi, E., Le Borgne, D., et al. 2007, A&A, 468, 33
Elbaz, D., Dickinson, M., Hwang, H. S., et al. 2011, A&A, 533, A119
Elmegreen, B. G., Bournaud, F., & Elmegreen, D. M. 2008, ApJ, 688, 67
Elmegreen, B. G., & Elmegreen, D. M. 2005, ApJ, 627, 632
Elmegreen, D. M., Elmegreen, B. G., Ravindranath, S., & Coe, D. A. 2007, ApJ, 658, 763
Fang, J. J., Faber, S. M., Koo, D. C., & Dekel, A. 2013, ApJ, 776, 63
Finlator, K., Davé, R., & Oppenheimer, B. D. 2007, MNRAS, 376, 1861
Finlator, K., Oppenheimer, B. D., & Davé, R. 2011, MNRAS, 410, 1703
Fontana, A., Santini, P., Grazian, A., et al. 2009, A&A, 501, 15
Förster Schreiber, N. M., Genzel, R., Bouché, N., et al. 2009, ApJ, 706, 1364
Fumagalli, M., Labbe, I., Patel, S. G., et al. 2013, arXiv:1308.4132
Fumagalli, M., Patel, S. G., Franx, M., et al. 2012, ApJL, 757, L22
Galametz, A., Grazian, A., Fontana, A., et al. 2013, ApJS, 206, 10
Genzel, R., Burkert, A., Bouché, N., et al. 2008, ApJ, 687, 59
Gobat, R., Strazzullo, V., Daddi, E., et al. 2012, ApJL, 759, L44
González, V., Bouwens, R., llingworth, G., et al. 2014, ApJ, 781, 34
Grogin, N. A., Kocevski, D. D., Faber, S. M., et al. 2011, ApJS, 197, 35
Guo, Y., Ferguson, H. C., Giavalisco, M., et al. 2013, ApJS, 207, 24
Guo, Y., Giavalisco, M., Cassata, P., et al. 2011, ApJ, 735, 18
Guo, Y., Giavalisco, M., Ferguson, H. C., Cassata, P., & Koekemoer, A. M. 2012, ApJ, 757, 120
Hopkins, P. F., Hernquist, L., Cox, T. J., & Kereš, D. 2008, ApJS, 175, 356
Hopkins, P. F., Hernquist, L., Cox, T. J., et al. 2006, ApJS, 163, 1
Ilbert, O., Salvato, M., Le Floc'h, E., et al. 2010, ApJ, 709, 644
Johansson, J., Thomas, D., & Maraston, C. 2012, MNRAS, 421, 1908
Karim, A., Schinnerer, E., Martínez-Sansigre, A., et al. 2011, ApJ, 730, 61
Kartaltepe, J. S., Dickinson, M., Alexander, D. M., et al. 2012, ApJ, 757, 23
Kauffmann, G., & Haehnelt, M. 2000, MNRAS, 311, 576
Kauffmann, G., Heckman, T. M., White, S. D. M., et al. 2003, MNRAS, 341, 54
Kauffmann, G., White, S. D. M., & Guiderdoni, B. 1993, MNRAS, 264, 201
Kaviraj, S., Cohen, S., Ellis, R. S., et al. 2013a, MNRAS, 428, 925
Kaviraj, S., Cohen, S., Windhorst, R. A., et al. 2013b, MNRAS, 429, L40
Kennicutt, R. C., Jr 1998, ARA&A, 36, 189
Kereš, D., Katz, N., Weinberg, D. H., & Davé, R. 2005, MNRAS, 363, 2
Kirkpatrick, A., Pope, A., Charmandaris, V., et al. 2013, ApJ, 763, 123
Koekemoer, A. M., Faber, S. M., Ferguson, H. C., et al. 2011, ApJS, 197, 36
Kravtsov, A. V., Klypin, A. A., & Khokhlov, A. M. 1997, ApJS, 111, 73
Kriek, M., van der Wel, A., van Dokkum, P. G., Franx, M., & Illingworth, G. D. 2008, ApJ, 682, 896
Kriek, M., van Dokkum, P. G., Franx, M., Illingworth, G. D., & Magee, D. K. 2009a, ApJL, 705, L71
Kriek, M., van Dokkum, P. G., Labbé, I., et al. 2009b, ApJ, 700, 221
Kriek, M., van Dokkum, P. G., Whitaker, K. E., et al. 2011, ApJ, 743, 168
Krist, J. 1995, in ASP Conf. Ser. 77, Astronomical Data Analysis Software and Systems IV, ed. R. A. Shaw, H. E. Payne, & J. J. E. Hayes (San Francisco, CA: ASP), 349
Krogager, J.-K., Zirm, A. W., Toft, S., Man, A., & Brammer, G. 2013, arXiv:1309.6316
Kümmel, M., Walsh, J. R., Pirzkal, N., Kuntschner, H., & Pasquali, A. 2009, PASP, 121, 59
Kurk, J., Cimatti, A., Daddi, E., et al. 2013, A&A, 549, A63
Lacy, M., Storrie-Lombardi, L. J., Sajina, A., et al. 2004, ApJS, 154, 166
Laidler, V. G., Grogin, N., Clubb, K., et al. 2006, in ASP Conf. Ser. 351, Astronomical Data Analysis Software and Systems XV, ed. C. Gabriel, C. Arviset, D. Ponz, & S. Enrique (San Francisco, CA: ASP), 228
Lee, J., & Yi, S. K. 2013, ApJ, 766, 38
Lee, S.-K., Idzi, R., Ferguson, H. C., et al. 2009, ApJS, 184, 100
Magdis, G. E., Daddi, E., Béthermin, M., et al. 2012, ApJ, 760, 6
Magnelli, B., Popesso, P., Berta, S., et al. 2013, A&A, 553, A132
Maraston, C., Pforr, J., Renzini, A., et al. 2010, MNRAS, 407, 830
McIntosh, D. H., Wagner, C., Cooper, A., et al. 2014, MNRAS, 442, 533
Moody, C. E., Guo, Y., Mandelker, N., et al. 2014, arXiv:1405.5266
Mullaney, J. R., Daddi, E., Béthermin, M., et al. 2012, ApJL, 753, L30
Muzzin, A., Marchesini, D., Stefanon, M., et al. 2013, ApJ, 777, 18
Naab, T., Johansson, P. H., & Ostriker, J. P. 2009, ApJL, 699, L178
Naab, T., Johansson, P. H., Ostriker, J. P., & Efstathiou, G. 2007, ApJ, 658, 710
Newman, A. B., Ellis, R. S., Andreon, S., et al. 2014a, ApJ, 788, 51
Newman, A. B., Ellis, R. S., Bundy, K., & Treu, T. 2012, ApJ, 746, 162
Newman, S. F., Buschkamp, P., Genzel, R., et al. 2014b, ApJ, 781, 21
Noeske, K. G., Weiner, B. J., Faber, S. M., et al. 2007, ApJL, 660, L43
Oser, L., Ostriker, J. P., Naab, T., Johansson, P. H., & Burkert, A. 2010, ApJ, 725, 2312
Pacifici, C., Charlot, S., Blaizot, J., & Brinchmann, J. 2012, MNRAS, 421, 2002
Pacifici, C., Kassin, S. A., Weiner, B., Charlot, S., & Gardner, J. P. 2013, ApJL, 762, L15
Papovich, C., Finkelstein, S. L., Ferguson, H. C., Lotz, J. M., & Giavalisco, M. 2011, MNRAS, 412, 1123
Papovich, C., Rudnick, G., Le Floc'h, E., et al. 2007, ApJ, 668, 45
Patel, S. G., Holden, B. P., Kelson, D. D., et al. 2012, ApJL, 748, L27
Patel, S. G., van Dokkum, P. G., Franx, M., et al. 2013, ApJ, 766, 15
Peng, C. Y., Ho, L. C., Impey, C. D., & Rix, H.-W. 2002, AJ, 124, 266
Pérez-González, P. G., Cava, A., Barro, G., et al. 2013, ApJ, 762, 46
Pérez-González, P. G., Egami, E., Rex, M., et al. 2010, A&A, 518, L15
Pérez-González, P. G., Rieke, G. H., Villar, V., et al. 2008a, ApJ, 675, 234
Pérez-González, P. G., Trujillo, I., Barro, G., et al. 2008b, ApJ, 687, 50
Pforr, J., Maraston, C., & Tonini, C. 2012, MNRAS, 422, 3285
Poggianti, B. M., Moretti, A., Calvi, R., et al. 2013, ApJ, 777, 125
Porter, L. A., Somerville, R. S., Primack, J. R., et al. 2014a, arXiv:1407.2186
Porter, L. A., Somerville, R. S., Primack, J. R., & Johansson, P. H. 2014b, arXiv:1407.0594
Reddy, N. A., Erb, D. K., Pettini, M., Steidel, C. C., & Shapley, A. E. 2010, ApJ, 712, 1070
Robertson, B., Bullock, J. S., Cox, T. J., et al. 2006, ApJ, 645, 986
Rodighiero, G., Cimatti, A., Gruppioni, C., et al. 2010, A&A, 518, L25
Rodighiero, G., Daddi, E., Baronchelli, I., et al. 2011, ApJL, 739, L40
Salim, S., Dickinson, M., Michael Rich, R., et al. 2009, ApJ, 700, 161
Salvato, M., Hasinger, G., Ilbert, O., et al. 2009, ApJ, 690, 1250
Salvato, M., Ilbert, O., Hasinger, G., et al. 2011, ApJ, 742, 61
Santini, P., Fontana, A., Grazian, A., et al. 2009, A&A, 504, 751
Santini, P., Rosario, D. J., Shao, L., et al. 2012, A&A, 540, A109
Saracco, P., Longhetti, M., & Gargiulo, A. 2010, MNRAS, 408, L21
Schaerer, D., de Barros, S., & Stark, D. P. 2011, A&A, 536, A72
Shen, S., Mo, H. J., White, S. D. M., et al. 2003, MNRAS, 343, 978
Silva, L., Maiolino, R., & Granato, G. L. 2004, MNRAS, 355, 973
Silverman, J. D., Mainieri, V., Salvato, M., et al. 2010, ApJS, 191, 124
Smail, I., Ivison, R. J., & Blain, A. W. 1997, ApJL, 490, L5
Somerville, R. S., Gilmore, R. C., Primack, J. R., & Domínguez, A. 2012, MNRAS, 423, 1992
Somerville, R. S., Hopkins, P. F., Cox, T. J., Robertson, B. E., & Hernquist, L. 2008, MNRAS, 391, 481
Springel, V., & Hernquist, L. 2005, ApJL, 622, L9
Springel, V., White, S. D. M., Jenkins, A., et al. 2005, Natur, 435, 629
Stark, D. P., Ellis, R. S., Bunker, A., et al. 2009, ApJ, 697, 1493
Stefanon, M., Marchesini, D., Rudnick, G. H., Brammer, G. B., & Whitaker, K. E. 2013, ApJ, 768, 92
Stern, D., Eisenhardt, P., Gorjian, V., et al. 2005, ApJ, 631, 163
Szokoly, G. P., Bergeron, J., Hasinger, G., et al. 2004, ApJS, 155, 271
Szomoru, D., Franx, M., Bouwens, R. J., et al. 2011, ApJL, 735, L22
Szomoru, D., Franx, M., & van Dokkum, P. G. 2012, ApJ, 749, 121
Targett, T. A., Dunlop, J. S., Cirasuolo, M., et al. 2013, MNRAS, 432, 2012

Thomas, D., Maraston, C., Bender, R., & Mendes de Oliveira, C. 2005, ApJ, 621, 673
Toft, S., van Dokkum, P., Franx, M., et al. 2007, ApJ, 671, 285
Tomczak, A. R., Quadri, R. F., Tran, K.-V. H., et al. 2014, ApJ, 783, 85
Tonini, C., Bernyk, M., Croton, D., Maraston, C., & Thomas, D. 2012, ApJ, 759, 43
Toomre, A. 1964, ApJ, 139, 1217
Tremonti, C. A., Moustakas, J., & Diamond-Stanic, A. M. 2007, ApJL, 663, L77
Trujillo, I., Conselice, C. J., Bundy, K., et al. 2007, MNRAS, 382, 109
Trump, J. R., Konidaris, N. P., Barro, G., et al. 2013, ApJL, 763, L6
Trump, J. R., Weiner, B. J., Scarlata, C., et al. 2011, ApJ, 743, 144
Tweed, D., Devriendt, J., Blaizot, J., Colombi, S., & Slyz, A. 2009, A&A, 506, 647
van der Wel, A., Bell, E. F., Häussler, B., et al. 2012, ApJS, 203, 24
van der Wel, A., Rix, H.-W., Wuyts, S., et al. 2011, ApJ, 730, 38
van Dokkum, P. G., & Brammer, G. 2010, ApJL, 718, L73
van Dokkum, P. G., Franx, M., Kriek, M., et al. 2008, ApJL, 677, L5
Vanzella, E., Cristiani, S., Dickinson, M., et al. 2008, A&A, 478, 83
Wang, T., Huang, J.-S., Faber, S. M., et al. 2012, ApJ, 752, 134
Whitaker, K. E., Kriek, M., van Dokkum, P. G., et al. 2012a, ApJ, 745, 179
Whitaker, K. E., Labbé, I., van Dokkum, P. G., et al. 2011, ApJ, 735, 86
Whitaker, K. E., van Dokkum, P. G., Brammer, G., & Franx, M. 2012b, ApJL, 754, L29
Whitaker, K. E., van Dokkum, P. G., Brammer, G., et al. 2013, ApJL, 770, L39
Wild, V., Heckman, T., & Charlot, S. 2010, MNRAS, 405, 933
Williams, C. C., Giavalisco, M., Cassata, P., et al. 2014, ApJ, 780, 1
Williams, R. J., Quadri, R. F., & Franx, M. 2011, ApJL, 738, L25
Williams, R. J., Quadri, R. F., Franx, M., et al. 2010, ApJ, 713, 738
Windhorst, R. A., Cohen, S. H., Hathi, N. P., et al. 2011, ApJS, 193, 27
Wuyts, S., Cox, T. J., Hayward, C. C., et al. 2010, ApJ, 722, 1666
Wuyts, S., Förster Schreiber, N. M., Genzel, R., et al. 2012, ApJ, 753, 114
Wuyts, S., Förster Schreiber, N. M., Lutz, D., et al. 2011a, ApJ, 738, 106
Wuyts, S., Förster Schreiber, N. M., van der Wel, A., et al. 2011b, ApJ, 742, 96
Wuyts, S., Labbé, I., Franx, M., et al. 2007, ApJ, 655, 51
Wuyts, S., van Dokkum, P. G., Franx, M., et al. 2009, ApJ, 706, 885
Xue, Y. Q., Luo, B., Brandt, W. N., et al. 2011, ApJS, 195, 10
Yesuf, H. M., Faber, S. M., Trump, J. R., et al. 2014, ApJ, in press (arXiv:1407.3834)
Zahid, H. J., Torrey, P., Kudritzki, R. P., et al. 2013, MNRAS, 436, 1852